# A non-equilibrium slurry model for planetary cores with application to Earth's F-layer

A. M. Walker, C. J. Davies, A. J. Wilson and M. I. Bergman

Addresses: Department of Earth Sciences, University of Oxford, South Parks Road, Oxford, OX1 3AN, UK, School of Earth and Environment, University of Leeds, Leeds, LS2 9JT, UK, Bard College at Simon's Rock, Great Barrington, MA 01230, USA. email: andrew.walker@earth.ox.ac.uk

**Author for correspondence:**
A. M. Walker
e-mail:
andrew.walker@earth.ox.ac.uk

# A non-equilibrium slurry model for planetary cores with application to Earth's F-layer

A. M. Walker[1,a], C. J. Davies[2,b], A. J. Wilson[2,c] and M. I. Bergman[3]

[1]Department of Earth Sciences, University of Oxford, South Parks Road, Oxford, OX1 3AN, UK
[2]School of Earth and Environment, University of Leeds, Leeds, LS2 9JT, UK
[3]Bard College at Simon's Rock, Great Barrington, MA 01230, USA
[a]https://orcid.org/0000-0003-3121-3255
[b]https://orcid.org/0000-0002-1074-3815
[c]https://orcid.org/0000-0002-6602-0990

Slurry regions may exist in the cores of several terrestrial bodies and are expected to influence the dynamics of deep planetary interiors and the viability of maintaining global magnetic fields. Here we develop a two-component slurry model of the lowermost outer core of the Earth (the F-layer). In contrast to most previous models of slurries in planetary cores, we explicitly model the physics controlling the nucleation, growth, and sinking of individual iron crystals and do not assume that the layer is in phase equilibrium. We assume that falling crystals do not interact and that the temperature and the overall composition are imposed, which allows us to solve for the volume fraction of solid in the layer and the size distribution of crystals. Models that produce a plausible heat budget and density excess compared to the bulk core yield a solid fraction that is far below that predicted by phase equilibrium and a crystal size distribution dominated by the smallest particles with a maximum particle radii of 3 cm. The model can be used to understand the role of non-equilibrium effects in other planetary cores.

# 1. Introduction

Interactions between solids and liquids are crucial for determining the thermal, chemical and magnetic evolution of the cores of terrestrial planets. Slow cooling of Earth's liquid core combined with high pressure conditions leads to freezing at the planet's centre, with rejection of light elements from the solid providing a main power source for the modern geomagnetic field [1]. However, the nature of this freezing is debated, with suggestions including direct freezing and dendritic growth [2], heterogeneous freezing and melting leading to inner core translation [3–5], and the possibility that iron crystallises and falls out of the liquid leading to growth by sedimentation [6, 7]. In contrast, theoretical and experimental work suggests that the cores of smaller bodies such as the Moon, Mars and Ganymede will freeze from the top down, producing a slurry layer near the top of the core in which a low volume fraction of heavy iron particles freeze out of the liquid and sink, remelting in the deeper core [8–14]. Modelling based on Fe-FeS alloys indicates that this "iron snow" regime significantly affects core evolution, for example through the formation of stable chemical stratification of S-rich liquid across the slurry layer and enhanced power for magnetic field generation arising from the sinking and remelting of solid particles [10, 12].

Several studies have argued that another slurry region exists at the base of Earth's liquid core [7, 15–20], explaining a low-velocity layer above inner core boundary (ICB). This low-velocity layer is a robust feature of seismic models of the outer core found in some one-dimensional reference models [21, 22] with additional evidence coming from targeted studies of body waves that propagate through the deep outer core or diffract along the ICB [e.g. 23–27]. These studies, reviewed in [28], provide strong evidence that lowermost 150 km [21, 23] to 400 km [27] of the liquid core has anomalously low P-wave velocity. This differs from models such as PREM [29], which closely follow an adiabatic density profile to the inner core boundary (ICB). The non-adiabatic P-wave velocity has been interpreted as a density stratification [30] of the liquid core. Here, we follow modern usage and call this layer the "F-layer", noting that originally this term was used for a thinner and lower-velocity layer. The excess density in the F-layer challenges our understanding of Earth's core because the light elements that are supposed to power field generation must be able to rise through the F-layer without disturbing the stratification.

The F-layer cannot be explained by a thermal boundary layer or a pure iron slurry [6], while a high solid fraction in the layer (reflecting a mushy zone) is also unacceptable as it would be seismically detected. Asymmetric melting and freezing of the inner core due to convective translation [3] may produce a dense layer of light-element-depleted fluid that envelops the inner core [4], which may explain the F-layer though this requires a much lower inner core thermal conductivity than obtained by most recent studies [e.g. 31] or some forcing from the outer core [32]. A slurry model of the F-layer is appealing because it predicts seismic velocities and density contrasts that are consistent with observations [19], while providing a self-consistent explanation for the flux of light elements into the overlying bulk core [7] and being compatible with the upward revision of the thermal conductivity of iron alloys [31, 33, 34]. In the model of Wong et al. [19] the temperature profile in the F-layer is destabilising and hence the stratification is driven by a radial increase in oxygen concentration. However, in common with all current snow/slurry models of planetary cores, this slurry F-layer model assumes thermodynamic equilibrium: there is no barrier to the nucleation, growth or melting of solids in the liquid. Here we construct a non-equilibrium model of the F-layer, under the assumption that it represents a slurry, in order to explore how departures from equilibrium could influence our understanding of the dynamics and evolution of slurries in planetary cores.

The common assumption of phase equilibrium means that the solid volume fraction, $\phi$, responds instantly to changes in temperature, $T$, pressure, $P$, and composition of the liquid, $X^L$ (where $X^L$ is mole fraction with $X^L = 1$ indicating pure Fe and $X^L = 0$ pure FeO). This makes it possible to keep track of $\phi$ and thus the contribution of the slurry layer to the thermal evolution of the planet, but extraction of information such as the size and settling velocity of the

crystals requires additional assumptions [10]. Solomatov and Stevenson [35] developed a theory for crystal nucleation and growth in a vigorously convecting silicate magma ocean but this does not readily translate to the fundamentally different conditions in planetary cores. Loper [36] did produce a non-equilibrium slurry theory by introducing a parameter to allow for small deviations from equilibrium, which represents the physics occurring at the scale of single iron particles below the continuum scale adopted by the rest of the theory. However, this approach has not been used to explore the behaviour of planetary cores.
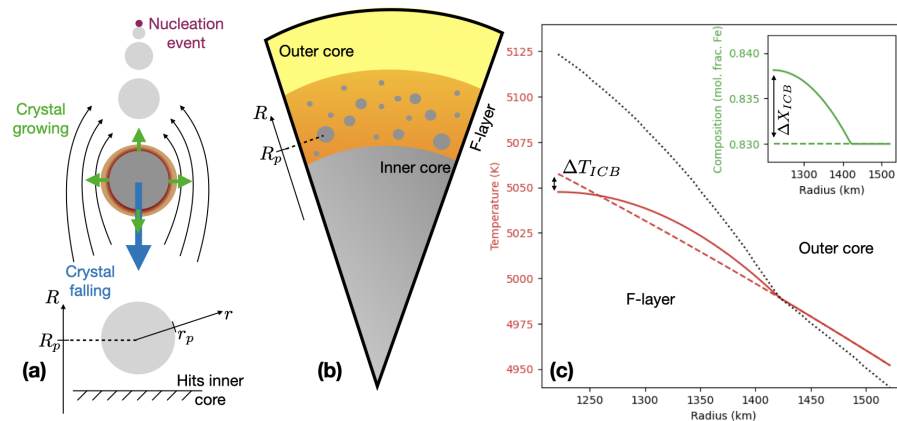


**Figure 1.** Illustration of the model setup. We focus on the small scale physics controlling the formation, falling and growth of single iron crystals (a) before combining these into a model of the collective behaviour of the F-layer (b). We illustrate the two 1-dimensional coordinate systems used in this work. One (denoted $r$) has an origin at the center of a single particle with radius $r_p$. The second ($R$) has an origin at the center of the Earth with a particle position denoted $R_p$ (a full list of the symbols used throughout this paper can be found in the Supplementary Information). Example temperature (red lines) and compositional (green lines) profiles relevant to this layer are shown in (c) alongside the liquidus temperature (black dotted line). In the outer core above the F-layer the composition is constant and the temperature follows an adiabatic profile (these are extrapolated as dashed lines inside the F-layer). The temperature intersects the liquidus at the top of the 200 km thick F-layer and below this the composition and temperature are parameterised by a second-order polynomial that differs by $\Delta T_{ICB}$ and $\Delta X_{ICB}$ from the extrapolation at the inner core boundary.

In this paper we develop a non-equilibrium model of Earth's F-layer as an iron snow zone built from the behaviour of single iron particles as they grow and fall towards the inner core boundary (Figure 1). We consider the combined effect of nucleation and growth as well as the important coupling between fluid dynamics of falling particles and thermodynamics of a two phase region. Our model does not impose thermodynamic equilibrium (although solutions may be in equilibrium) and yields rich information on the state of the layer. Section 2 describes a thermodynamic model of the Fe-FeO system, valid at the high $P$ and $T$ conditions of Earth's core, that is used to determine the chemical potential differences that drive particle nucleation and growth and the extent of departures from equilibrium. This choice of chemistry (which can be easily changed in our implementation) is consistent with the seismically-inferred density difference between inner and outer core [37] and allows us to neglect the possibility of light elements partitioning into the solid phase, which also proves to be a useful simplification. Section 3 details the processes we consider to determine the fluid dynamics of a single pre-existing iron particle, the particle's falling velocity and properties of the momentum and compositional

boundary layers that develop in the liquid adjacent to the solid interface, and how these couple to the particle growth. This treatment of iron particles involves additional assumptions, principally that the fluid in the slurry layer is density stratified, that particles are spherical and that they do not interact with each other either via physical collisions or induced fluid flow. Section 4 describes how we consider the formation of solid particles within the slurry and involves the assumptions of classical nucleation theory (where we find it necessary to invoke preexisting 'dust' as nucleation sites). In section 5 we describe the collective behaviour of particles as they nucleate and grow while falling through the F-layer within a 1D model. This involves the imposition of a temperature and compositional profiles for the liquid and the implicit assumption that the processes governing the approach to equilibrium in the F-layer occur on a timescale much faster than secular changes to the temperature or composition of the overlying outer core. This 1D model produces a size distribution, number density and lifespan of groups of solid particles that nucleate at a particular radius and fall through the F-layer. From this information, we compute the growth rate of the inner core (with the assumption that the inner core only grows by sedimentation of falling particles) alongside the density profile (including contributions from the solid volume as well as the composition and temperature of the liquid) and heat and oxygen production in the layer that is released upwards into the outer core. Finally, in section 6, we search for models that match constraints from seismology and the thermal evolution of the Earth, describe the kinds of solutions that are acceptable within these constraints, and consider potential extensions of this work to other planetary cores and paths to lifting of some key assumptions and integrating our results within other models of the core.

## 2. An iron-oxygen thermodynamic model for the F-layer

In common with most existing models of slurries in planetary cores, we start by simplifying the composition of the core and consider an alloy of iron and a light element which partitions strongly into the liquid phase on crystallisation. In the limit of complete partitioning this approximation (the "constant solid composition" approximation of [17]) means there is no need to track the composition of the solid in the slurry. For Earth, oxygen is a common choice of light element [33] because it is cosmochemically abundant, expected to partition into the core during planetary differentiation, and, as opposed to S and Si, is likely to produce a density jump at the inner core boundary as required by seismology [38]. Komabayashi [39] produced a thermodynamic description of the Fe-FeO alloy system at high temperature and pressure that is suitable for use in our model and in which oxygen does not enter the solid iron phase. However, we note that it is not possible for the core to be formed entirely of an Fe-O alloy as this does not account for the density of the inner core and the eutectic for this system is colder than the expected temperature of the inner core boundary. Nevertheless, the simple system is well suited to our needs and demonstrates the power of the model we develop.

At equilibrium, slurry layers in metallic planetary cores can exist over a range of pressure-temperature conditions because of the presence of two phase regions in metal alloy phase diagrams. An example for the prototypical Fe-FeO system calculated for plausible F-layer pressure-temperature-composition conditions is shown in Figure 2. The equilibrium assemblage for a composition that falls within the region bounded by the liquidus, the solidus and the eutectic temperature (marked 'two phase region') will, on the terrestrially relevant Fe rich side of the eutectic point considered here, be a mixture of solid iron and a liquid Fe-O alloy with composition enriched in O compared to the bulk. We use the thermodynamic model of Komabayashi [39] to describe the free energy of pure solid Fe, stoichiometric FeO and a Fe-O liquid. In this model, the volumes of the end-members are described by Vinet-Anderson-Grüneisen equations of state to capture the effect of pressure and pressure-dependent thermal expansion. This yields the end-member molar volumes and thus the densities of the (pure iron) solid, $\rho^{\mathrm{S}}$, and of liquid Fe and FeO all as a function of $P$ and $T$. These are combined with a polynomial representation of the free energies as a function of temperature at fixed volume to give the chemical potential of iron in the end-members, $\mu_{\mathrm{Fe}}^{\mathrm{S}}(P, T, X^{\mathrm{S}} = 1)$ and $\mu_{\mathrm{Fe}}^{\mathrm{L}}(P, T, X^{\mathrm{L}} = 1)$. Liquid Fe and FeO (under these high

pressure conditions) are assumed to form an ideal solution [39] and therefore the liquid density, $\rho^{\text{L}}$, for any composition $X^{\text{L}}$, is found by linearly interpolating between end members and the chemical potential difference between solid and liquid is

$$\Delta\mu_{\text{Fe}}(P, T, X^{\text{L}}) = \mu_{\text{Fe}}^{\text{S}}(P, T, X^{\text{S}} = 1) - \left[ \mu_{\text{Fe}}^{\text{L}}(P, T, X^{\text{L}} = 1) + R_g T \ln X^{\text{L}} \right], \quad (2.1)$$

where $R_g$ is the gas constant and the final term represents the entropy of mixing (with the positive sign resulting from a decrease in entropy with increasing iron content in the liquid). In order to efficiently evaluate the volume of each phase (and thus the densities and chemical potential) as a function of pressure, we use an approximate inverse of the Vinet EOS to avoid the need for a numerical solution at each pressure [40]. As shown in Figure 2, for a given range of pressures and temperatures, the iron fraction of the liquid, $X^{\text{eq}}$, in equilibrium with solid iron can be found from this thermodynamic model by searching for the composition where $\Delta\mu_{\text{Fe}}(P, T, X^{\text{L}}) = 0$. This defines the liquidus.

For a given composition of the liquid and bulk composition, $X^{\text{tot}}$, it is possible to evaluate the mole fraction solid, $\mathcal{X}$, by conserving the total composition of the system:

$$\mathcal{X} = 1 - \frac{1 - X^{\text{tot}}}{1 - X^{\text{L}}}. \quad (2.2)$$

Setting $X^{\text{L}} = X^{\text{eq}}$ in Equation 2.2 yields the lever rule and the equilibrium mole fraction solid, $\mathcal{X}^{\text{eq}}$. This is shown by the shading in Figure 2 and the difference between $\mathcal{X}$ and $\mathcal{X}^{\text{eq}}$ is one way to measure departure from equilibrium. Since we know the volumes of the components, it is straightforward to convert from $\mathcal{X}$ (and $\mathcal{X}^{\text{eq}}$), to volume fraction solid, $\phi$, and the equilibrium volume fraction, solid $\phi^{\text{eq}}$, which are more amenable to calculation. An analogous approach can us used to probe the FeO side of the phase diagram. While this is unlikely to be directly relevant to the F-layer, it may pertain to small planetary bodies such as Ganymede [41].
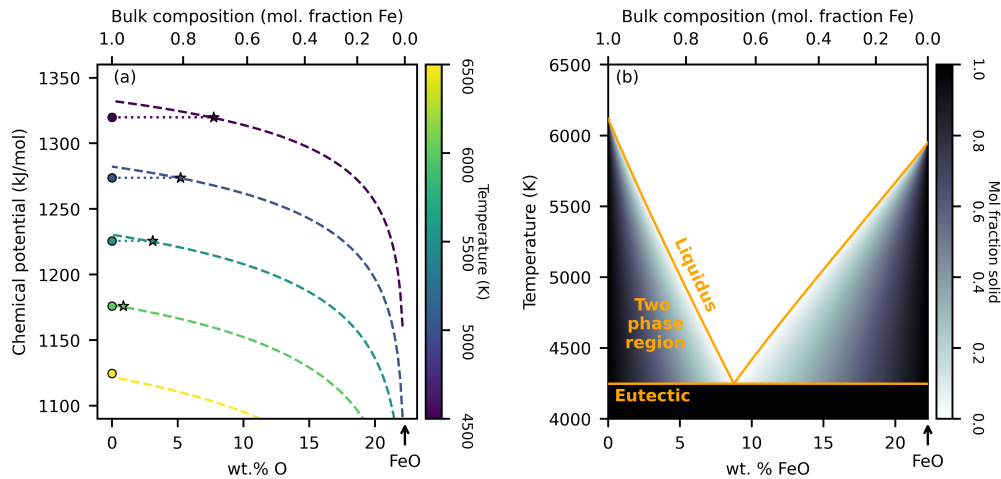


**Figure 2.** Equilibrium properties of the Fe-FeO system computed from [39] at 330 GPa. (a) The chemical potential of liquid FeO mixtures (dashed lines) and the pure solid Fe chemical potential (circles) coloured by temperature. Dotted tie lines connect solid Fe with the equilibrium liquid mixture for temperatures within the two phase region. At 6500 K solid Fe is unstable compared to a pure Fe liquid. (b) Calculated phase diagram where phase boundaries (liquidus and eutectic) are shown (orange lines) and the solid Fe – liquid FeO two-phase region relevant to our slurry model is labeled. The equilibrium solid fraction is indicated by the shading.

The equilibrium thermodynamics summarised above allow the relationship between solid fraction, composition, temperature and pressure to be described in models of slurries. This

amounts to models where the temperature and pressure define the composition of the liquid or, equivalently, where knowing the composition and pressure defines the temperature via a liquidus relation. Because this equilibrium is maintained by the rapid creation or removal of solid this approximation is often known as the "fast melting" approximation (see [17]) and it is this that allows a parameterised liquidus (rather than a thermodynamic description of melting) to appear in slurry models [7, 10, 12, 19]. It is this approximation that we seek to lift. We can do this because, as well as allowing the calculation of the equilibrium phase diagram, a thermodynamic model provides access to the driving force, $\Delta\mu_{\mathrm{Fe}}$, for the processes which determine how quickly a non-equilibrium system will move towards equilibrium. In a slurry with smaller $\phi$ than predicted by Equation 2.2, large negative values of $\Delta\mu_{\mathrm{Fe}}(P, T, X^{\mathrm{L}})$ will tend to drive faster growth and higher nucleation than small values but this driving force must compete with kinetic effects (diffusion and collision rate of atoms), and can only operate for a limited time period while any solid falls out of the liquid. This makes the thermodynamic model summarised in Equation 2.1 key to our non-equilibrium description of the F-layer, despite the fact that the model is parameterised, in part, to reproduce equilibrium experiments.

# 3. A model of a falling growing iron particle

Before describing the properties of the whole slurry layer, we develop a model of a single solid iron particle falling through a stationary liquid iron alloy within the two phase region. The rate $\mathrm{d}r_p/\mathrm{d}t$ at which a spherical particle of radius $r_p$ grows or shrinks as it falls controls how quickly it can contribute to phase equilibrium within the layer while its falling velocity $w_p$ ($= -\frac{\mathrm{d}R_p}{\mathrm{d}t}$ as $R$ increases upwards) controls how long it has to contribute to this process. Because of the physical processes described below we expect the falling velocity to depend on the particle size and the growth rate to depend on the falling velocity, so we evolve the position and size of the particle together by integrating a pair of coupled ordinary differential equations. Our task is to describe the coupling of $R_p$ and $r_p$ and to evaluate $R_p(t)$ and $r_p(t)$ where time, $t$, is measured from the instant the particle first forms. Throughout we assume that the F-layer is stratified, that the total solid fraction is low (so particles do not interact via collisions or by closely approaching each other; this is expected in a slurry) and that thermal diffusion is sufficiently fast [42] to maintain thermal equilibrium (such that we can impose the temperature). For the purpose of this section (where we only consider a single iron particle) we impose constant temperature, pressure and liquid composition, although we allow these to vary with $R$ in later sections.

## (a) Falling velocity

Time-dependent 3D solutions of the Navier-Stokes equations for a fluid containing a large number of solid particles are computationally inaccessible at the conditions of planetary cores. To enable a flexible and fast representation of solid-liquid fluid dynamical interactions we therefore utilise scaling laws that describe the gross properties of the particle velocity and the boundary layers surrounding falling particles.

Particles in the slurry are assumed to be denser than the stratified liquid and will quickly accelerate to fall at their terminal velocity. The simplest estimate of the particle velocity is based on Stokes flow, which gives the terminal velocity of the particle by balancing buoyancy and drag forces and applies at low Reynolds number, $Re$, defined as:

$$Re = \frac{2r_p|w_p|}{\nu^{\mathrm{L}}}, \tag{3.1}$$

where $\rho^{\mathrm{L}}$ and $\nu^{\mathrm{L}}$ are the liquid density and kinematic viscosity, respectively. In this classical regime $w_p = w_{\mathrm{stokes}} = \frac{2}{9}(\rho^{\mathrm{S}} - \rho^{\mathrm{L}})gr_p^2/(\nu^{\mathrm{L}}\rho^{\mathrm{L}})$, where $g$ is gravity. As $w_p$ (and $Re$) increases the drag experienced by the sphere is enhanced compared to the Stokes solution. We utilise an

empirical relation for the drag coefficient valid for $Re \leq 3 \times 10^5$ [43–45],

$$C_D = \frac{24}{Re}(1 + 0.15Re^{0.687}) + \frac{0.42}{1 + 42500Re^{-1.16}}, \tag{3.2}$$

in terms of which the falling velocity is

$$w_p = -\frac{\mathrm{d}R_p}{\mathrm{d}t} = \sqrt{\left(\frac{8}{3}\frac{(\rho^S - \rho^L)gr_p}{\rho^L C_D}\right)}. \tag{3.3}$$

Because $Re$ depends on $w_p$, Equations 3.1 and 3.3 are solved self consistently as described in [45].

To represent the boundary layer dynamics, we first note that the compositional boundary layer in the solid and the thermal boundary layers on either side of the particle-fluid interface are absent by assumption. The momentum boundary thickness in the liquid, $\delta_u$, is required to determine the thickness of the chemical boundary layer in the liquid, $\delta_C$. To describe $\delta_u$ and $\delta_C$ we use results from Inman et al. [46], who numerically simulated the incompressible axisymmetric flow arising from an isolated particle sinking through a stabilising linear chemical gradient. A stabilising background gradient has been obtained in recent equilibrium models of the F-layer [19] and snow zones [10]. In this configuration the dynamics are described by the Schmidt, chemical Péclet, and Froude numbers, which are defined respectively as

$$Sc = \frac{\nu^L}{D^L}, \quad Pe_C = \frac{2r_p|w_p|}{D^L} = ScRe, \quad Fr = \frac{|w_p|}{N_{BV}r_p}, \tag{3.4}$$

where $D^L$ is the oxygen diffusion coefficient in the liquid and $N_{BV}$ is the Brunt–Väisälä frequency

$$N_{BV}^2 = -\frac{g}{\rho}\frac{\partial\rho'}{\partial r} \approx -\frac{g_m}{\rho_m}\frac{\rho_t' - \rho_b'}{R_t - R_b}, \tag{3.5}$$

which increases as the layer becomes more strongly stratified. Here $\rho'$ is the the density deviation from the adiabatic and chemically well-mixed state and the right-hand side approximates $N_{BV}$ by quantities in the middle (subscript $m$), top (subscript $t$) and base (subscript $b$) of the layer. In the geophysically relevant limit of $Sc \gg 1$ [42] the regimes depend on $Fr$ and $Re$. At high $Fr$ (weak stratification) and $Re < 10^{-2}$ the momentum boundary layer is weak or absent because advection cannot balance viscous diffusion in the boundary layer equation and the only length-scale in the problem is $2r_p$. The results of [46] suggest that the chemical boundary is also weak or absent at $Pe_C \sim 10$, which corresponds to $Re \sim 10^{-2}$ for $Sc \sim 1000$. At higher $Pe_C$ a chemical boundary layer of thickness $\delta_C$ at the particle equator develops in which the chemical advection and diffusion are approximately in balance. The mechanical boundary thickness $\delta_u$ depends on $Re$: $\delta_u/2r_p \sim 1$ at $10^{-2} \leq Re \leq 10^2$ (see Figure 7b of [46]); $\delta/2r_p \sim Re^{-0.5}$ for $Re > 200$, i.e. the classical balance between viscosity and inertia. In the low $Fr$ (strong stratification) regime the same logic is applied except that for $Re \geq 10^{-2}$, $\delta_u$ is estimated based on a balance between viscosity and buoyancy in the momentum equation [46]. With these considerations the chemical boundary layer thicknesses in the weak stratification ($Fr > 10$), regime are

$$\delta_C = \begin{array}{ll} 2r_p & Re < 10^{-2}, \\ 0.215Re^{-1/3}2r_p & 10^{-2} \leq Re \leq 10^2, \\ 0.464Re^{-1/2}2r_p & Re > 10^2, \end{array} \tag{3.6}$$

while in the strong stratification regime ($Fr \leq 10$) they are

$$\delta_C = \begin{array}{ll} 2r_p & Re < 10^{-2}, \\ 0.1Re^{-1/2}2r_p & Re \geq 10^{-2}. \end{array} \tag{3.7}$$

In these equations the prefactors are determined by continuity of mechanical and compositional boundary layer thicknesses at the regime boundaries as in [47].

Calculated falling velocities, boundary layer thickness and scaling regime information are shown as a function of $r_p$ for solid and liquid properties expected close to the ICB in Figure 3. From the nanometer size expected after nucleation small particles experience laminar flow,
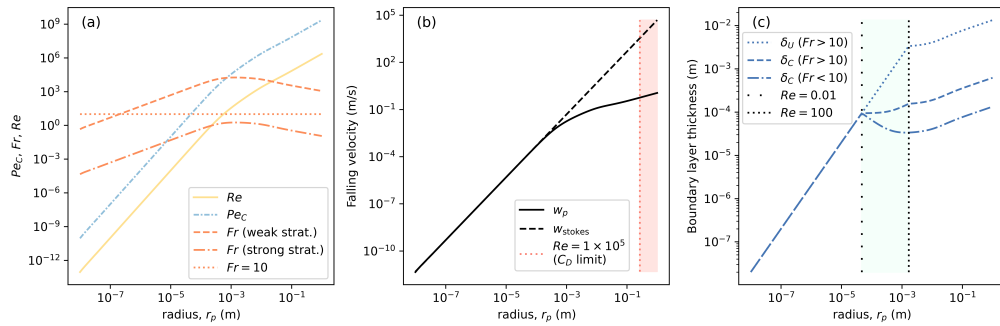
**Figure 3.** Dynamical regime, falling velocity and boundary layer thickness for a iron particle falling through a stratified liquid with parameters relevant to the F-layer ($\rho^S = 12700$ kg m$^{-3}$, $\rho^L = 12100$ kg m$^{-3}$, $g = 4.4$ m s$^{-2}$, $D^L = 1 \times 10^{-9}$ m$^2$ s$^{-1}$ and $\nu^L = 1 \times 10^{-6}$ m$^2$ s$^{-1}$). (a) $Re$ (yellow) and $Pe_C$ (blue) and $Fr$ (orange, dashed for $N_{BV} = 10^{-3}$ Hz and dash-dots for $N_{BW} = 10$ Hz) are calculated self consistently and determine the dynamical regime, with $Fr = 10$ indicated. (b) Falling velocity (solid line) and Stokes velocity (dashed line) showing the divergence at larger particle radii. The vertical line and pink shading corresponds to $Re \geq 3 \times 10^5$, the upper bound on the empirical scaling for the drag coefficient. (c) Momentum (dotted line) and chemical (dashed for $N_{BW} = 10^{-3}$ and dash-dots for $N_{BW} = 10$ Hz) boundary layer thickness. Vertical dotted lines showing the intermediate and large $Re$ regime transitions.

have a relatively large boundary layer thickness and fall at the classical Stokes velocity. As the particle grows to the ten to 100 micron range it enters the intermediate $Re$ regime, develops a relatively thinner boundary layer and gradually slows down compared to the Stokes prediction. The deviation between the Stokes falling velocity and the self-consistent calculation is clear by the time the particle grows to mm size and enters the high $Re$ regime. For these parameters, if the particle were to grow beyond 25 cm the empirical drag coefficient would no longer be valid. This corresponds to falling velocities in the m/s range, where particles traverse the whole F-layer in a few days. Figure 3 also shows the difference in boundary layer behaviour for a particle falling through a weak chemical stratification (high $Fr$, $N_{BW} = 10^{-3}$ Hz) and a strong stratification (low $Fr$, $N_{BW} = 10$ Hz). For the Earth, the difference between PREM (which has an adiabatic density in the outer core [48]) and AK135-F (where the base of the outer core shows stable stratification, [49]) predicts $N_{BW} \sim 1 \times 10^{-4}$ Hz at the base of the F-layer. We thus expect boundary layers for particles to be more accurately represented by the weakly stratified (low $Fr$) scaling.

## (b) Growth rate

The rate of particle growth depends primarily on three factors: the thermodynamic driving force $\Delta\mu_{\text{Fe}}$; surface kinetics, reflecting the fact that particles cannot grow faster than the rate at which atoms arrive at the interface and arrange themselves into the solid structure; and, compositional variations in the adjacent liquid. The first two factors are typically described by models of the form

$$\frac{dr_p}{dt} = k(T)\left[1 - \exp\left(\frac{\Delta\mu_{\text{Fe}}(P, T, X^L)}{R_g T}\right)\right], \tag{3.8}$$

where $k(T)$ is a kinetic function, and $\Delta\mu_{\text{Fe}}$ is defined in Equation 2.1. Zero growth rate occurs at equilibrium, i.e. when $\Delta\mu_{\text{Fe}} = 0$.

The growth rate of iron under core conditions, and thus the appropriate parameters of Equation 3.8 are not known. There are at least three groups of theories for $k(T)$ for pure metals, those which assume diffusion controlled kinetics [50, 51], those which assume collision-controlled kinetics [52], and those which assume density fluctuations in the liquid control the kinetics of growth [53]. Atomic scale simulations of six $fcc$ metals suggests that a temperature independent

kinetic factor (i.e. $k(T) = k_0$) with large magnitude (140 to 650 m/s) gives a good description of the growth kinetics to large undercooling [54] and we assume similar behaviour holds for $hcp$ iron at ICB conditions. However, in our two component system it is evident that movement of oxygen away from the growing interface must play a role. Oxygen will need to diffuse through the boundary layer set up by the falling particle and the thickness of this layer depends on the particle size as discussed above. Existing theories appealing to diffusion to define $k(T)$ are not well suited to this situation, so we proceed by separating the kinetic control on particle growth into two contributions setting $k(T) = k_0$ [54] and treating oxygen diffusion separately.

Compositional variations in the boundary layer arise due to the exclusion of oxygen from the solid as the particle grows. As described in the Supplementary Information, conservation of mass leads to a relationship between the particle growth rate and the gradient of the composition of the liquid at the particle interface:

$$\left. \frac{\mathrm{d}X(r)}{\mathrm{d}r} \right|_{r=r_p} = \frac{X(r_p)}{D^{\mathrm{L}}} \frac{\mathrm{d}r_p}{\mathrm{d}t}. \tag{3.9}$$

Supported by the results of [46], we assume that the boundary layer structure is linear, increasing from $X(r_p)$ at the interface to the bulk liquid composition, $X(r_p + \delta_C) = X^{\mathrm{L}}$, at and beyond the outer edge of the boundary layer. Using Equation 3.8, Equation 3.9 becomes

$$\left. \frac{\mathrm{d}X(r)}{\mathrm{d}r} \right|_{r=r_p} \approx \frac{X^{\mathrm{L}} - X(r_p)}{\delta_C} = \frac{k_0 X(r_p)}{D^{\mathrm{L}}} \left[ 1 - \exp\left( \frac{\Delta\mu_{\mathrm{Fe}}\left(P, T, X(r_p)\right)}{RT} \right) \right]. \tag{3.10}$$

For a given $\delta_C$ (which does not depend on $X(r)$) and $X^{\mathrm{L}}$, this relation determines the particle growth rate that is consistent with the liquid composition and its gradient at the interface.

Figure 4a shows the variation in growth rate as a function of solid fraction with fixed bulk composition for different values of $k_0$ using Equation 3.8. At $\phi = 0$, $\Delta\mu_{\mathrm{Fe}}$ is large and negative and the growth rate is set by $k_0$. Increasing solid fraction evolves the system towards the equilibrium composition at which point all curves reach zero growth rate ($\Delta\mu_{\mathrm{Fe}} = 0$), which occurs at a single composition at the fixed $P$ and $T$ conditions shown. The compositions highlighted in Figure 4a are used in Figures 4b and c to demonstrate the variation of $dr_p/dt$ and $X(r_p)$ with boundary layer thickness as determined by Equation 3.10. To understand the behaviour it is helpful to combine Equations 3.8 and 3.10 into the form

$$X^{\mathrm{L}} = X(r_p) \left[ 1 + \frac{\delta_C}{D} \frac{\mathrm{d}r_p}{\mathrm{d}t} \right] \tag{3.11}$$

and note that, in this analysis, $dr_p/dt$ is a function only of $X(r_p)$ because $P$ and $T$ are fixed (see the definition of $\Delta\mu_{\mathrm{Fe}}$ in Equation 2.1). At small $\delta_C$, the first term in brackets in (3.11) is dominant, implying $X(r_p) \sim X^L$ and a fast growth rate. As $\delta_C$ is increased at fixed $D$ the two terms in the brackets in (3.11) become comparable, requiring $X(r_p)$ to decrease compared to $X^{\mathrm{L}}$, which reduces the growth rate as seen in Figures 4 b and c. Physically, the large growth rate that arises when the system is far from equilibrium is associated with large diffusive flux across the chemical boundary layer, which is required to bring the system towards equilibrium. At equilibrium $dr_p/dt = 0$ and $X^L = X(r_p)$ corresponding to zero diffusive flux.

## (c) A single falling and growing particle

The time evolution of the size and position of a falling particle is described by the pair of coupled ODEs (Equations 3.9 and 3.3) for a particle that starts with initial radius $r_0$ at position $R_0$. We solve these together as an initial value problem making use of the 'RK45' Runge-Kutta method [55] as implemented in the SciPy library [56], where the dynamical time stepping is essential to efficient solution. In detail, at each Runga-Kutta step the growth rate and falling velocity is found as follows:

(i) Calculate $\rho^{\mathrm{S}}$, $\rho^{\mathrm{L}}$ and $\Delta\mu_{\mathrm{Fe}}$ from $T$, $P$ and $X^{\mathrm{L}}$ as outlined in Section 2.
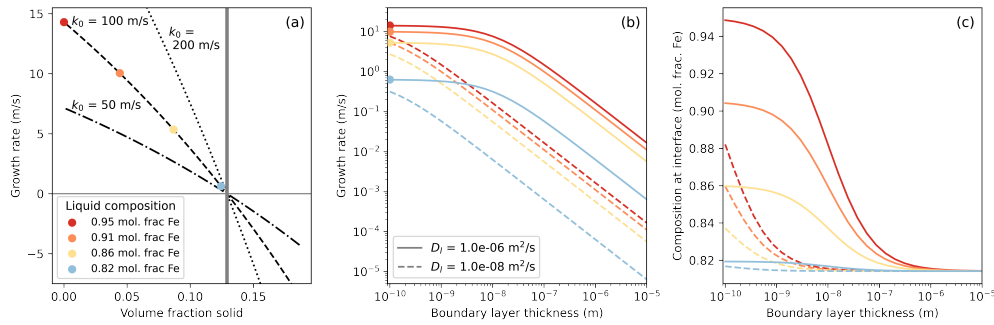
**Figure 4.** Calculated particle growth rate $dr_p/dt$ for bulk composition $X^{\text{tot}} = 5$ mol. % O, $T = 5000$ K and $P = 330$ GPa. (a) shows $dr_p/dt$ as a function of solid fraction $\phi$, neglecting boundary layer effects, using Equation 3.8. Vertical grey line denotes the equilibrium solid fraction at the chosen $P - T - X^{\text{tot}}$. Coloured symbols denote the liquid composition calculated from Equation 2.2 for the given $\phi$ and $X^{\text{tot}}$. (b) and (c) show $dr_p/dt$ and $X(r_p)$ as a function of fixed boundary layer thickness using the four liquid compositions marked in (a) calculated with Equation 3.10. Two values of the oxygen diffusivity are shown in solid and dashed lines. All coloured cases have $k_0$ set to 100 m/s.

(ii) Self consistently solve Equations 3.1–3.3 to find $Re$ and the particle falling velocity, $-\frac{\mathrm{d}R_p}{\mathrm{d}t}$.

(iii) Calculate the thickness of the chemical boundary layer from Equation 3.6.

(iv) Self consistently solve Equations 3.8–3.10 to find the growth rate, $\frac{\mathrm{d}r_p}{\mathrm{d}t}$, and liquid composition at the interface.

(v) With $\frac{\mathrm{d}R_p}{\mathrm{d}t}$ and $\frac{\mathrm{d}r_p}{\mathrm{d}t}$ in hand, update the position and size of the falling particle.

This process ends when the particle hits the ICB and yields interpolating polynomials describing the particle position and size, $R_p(t; R_0, r_0)$ and $r_p(t; R_0, r_0)$, as a function of time, where we explicitly represent the dependence on initial conditions following the semi-colon. These functions can be used to easily find the particle size as a function of position, $r_p(R_p; R_0, r_0)$. In addition to the thermodynamic parameterisation, this calculation requires knowledge of pressure, temperature, acceleration due to gravity, liquid viscosity, chemical diffusivity, the pre-factor for growth, and the composition of the liquid outside the boundary layer. Our implementation allows these to be fixed or to vary with $R$. Solutions for some cases with fixed parameters roughly corresponding to the F-layer on Earth are shown in Figure 5.

Particle evolution can be summarised by the transit time (the time taken to fall 200 km from the top to the bottom of the F-layer) and the final particle size just before it hits the ICB. The effect of two major controls on these summary measures, the liquid viscosity and oxygen diffusivity, are shown in Figure 5b. As oxygen diffusivity increases the particles grow faster and thus fall faster giving smaller transit times and larger final sizes. This can be seen by tracking any set of data points at fixed viscosity. Increasing viscosity at fixed oxygen diffusivity results in solutions that follow curved lines of fixed colour across Figure 5c. As expected, increasing the viscosity increases the drag, decreases the falling velocity and thus increases the transit time. However, for solutions with fixed oxygen diffusivity the final particle size is approximately independent of viscosity: the decreased falling velocity is balanced by a decreased growth rate. This can be explained by noting that, to leading order, $D^{\text{L}}$ and the $\delta_C$ scale in the same way with $Re$ and thus viscosity.

Having considered the controls on the evolution of a single iron particle, we now focus on particle nucleation before considering how they behave en-mass within the F-layer.

# 4. Nucleation

No model of a core slurry zone is complete without consideration of how the solid particles form, and this process is particularly important in allowing deviation from equilibrium. The basic
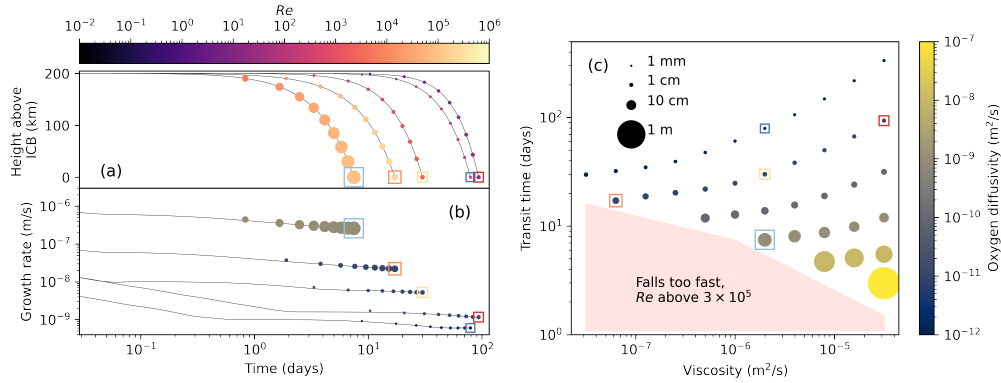
**Figure 5.** Summary of iron particle evolution during the process of falling through a 200 km thick layer of liquid iron containing 5 mol. % oxygen. Pressure is 330 GPa, temperature 5500 K, gravitational acceleration 5 ms$^{-2}$ and the initial particle size is $10^{-8}$ m. The position (a) and growth rate (b) of particles as a function of time as they fall through liquids with five different oxygen diffusivities and viscosities are shown with particle size indicated by symbol size (key in panel c) and $Re$ indicated by colour in (a; top colour bar). The colour of the squares around the terminal symbols indicate oxygen diffusivities (red, orange and yellow: $D^L = 1 \times 10^{-11}$; light blue: $D^L = 1 \times 10^{-9}$; dark blue: $D^L = 1 \times 10^{-12}$ m$^2$s$^{-1}$) and viscosities (yellow, dark blue and light blue: $\nu^L = 2 \times 10^{-6}$; red: $\nu^L = 3 \times 10^{-5}$; orange: $\nu^L = 6 \times 10^{-8}$ m$^2$/s). Results from a larger set of input parameters are summarised in terms of the total transit time of the particle and it's final size in (c) with the five cases shown in (a) and (b) highlighted by the same coloured squares. The symbol colours in (b) and (c) indicate oxygen diffusivity according to the color bar on the right hand side of the figure.

approach involves Classical Nucleation Theory (CNT), which accounts for the need for a liquid to cool sometimes significantly below its melting point (or liquidus temperature) before a solid can form [57]. The key idea is that spontaneous perturbations in the structure of the supercooled liquid will result in the formation of a nucleus of solid sufficiently large that the energy released on freezing (which scales with the volume of the nucleus) overcomes the energy penalty that accompanies the formation of an interface between the new solid and liquid (which scales with surface area). For a spherical nucleus of radius $r$, the energy change is:

$$\Delta G(r, P, T, X^{\mathrm{L}}) = \left[ \frac{4}{3}\pi r^3 g_{sl}(X^{\mathrm{L}}, P, T) + 4\pi r^2 \gamma \right] S(\theta) \tag{4.1}$$

where $g_{sl} = \Delta\mu_{\mathrm{Fe}}(P, T, X^{\mathrm{L}})\frac{\rho^{\mathrm{L}}}{56}$ is given by Equation 2.1 (in units of energy per unit volume), $\gamma$ is the excess energy caused by forming a solid-liquid interface (in units of energy per unit area), and the factor of 56 is the molar mass of iron. The function $S(\theta) = [2 - 3\cos(\theta) + \cos^3(\theta)]/4$, where $\theta$ is the wetting angle between the solid and the liquid, permits the consideration of heterogeneous nucleation (where a pre-existing solid exists) considered below. For homogeneous nucleation (formation of new solid without a pre-existing solid surface) $\theta = 180°$.

The critical size $r_c$ beyond which a spontaneously formed spherical nucleus will be more likely to grow than dissolve corresponds to the maximum of $\Delta G$

$$r_c(P, T, X^{\mathrm{L}}) = \frac{-2\gamma}{g_{sl}(P, T, X^{\mathrm{L}})} \tag{4.2}$$

and has energy

$$G(r_c(P, T, X^{\mathrm{L}})) = \frac{16\pi\gamma^3}{3g_{sl}(P, T, X^{\mathrm{L}})^2} S(\theta) \tag{4.3}$$

Heterogeneous nucleation reduces the energy barrier at $r_c$ for small wetting angles, such as those typically found in metals [58].
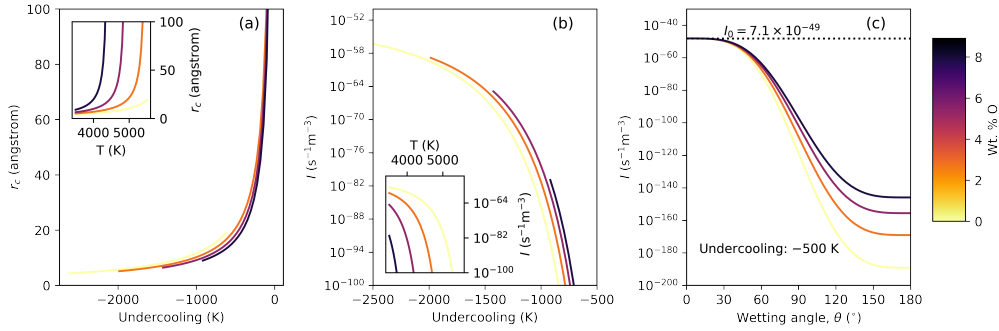
**Figure 6.** Critical nucleus size (a) and nucleation rate (b) for iron in an iron-oxygen supercooled liquid as a function of temperature and liquid composition. Calculations are performed at 330 GPa, with $\gamma = 1.08$ J m$^{-2}$, and $I_0 = 7.1 \times 10^{-49}$ s$^{-1}$ m$^{-3}$ [59]. In the main plots the temperature is shown in terms of undercooling below the liquidus temperature for each composition, while the insets show the same data in terms of absolute temperature which spreads out the curves (see text). The effect of wetting angle, $\theta$ for heterogeneous nucleation is show in in (c) for fixed 500 K undercooling. The nucleation rate approaches $I_0$ for small $\theta$.

Given a pre-factor that describes the rate at which liquid 'attempts' to form solid, $I_0$, CNT allows the calculation of the nucleation rate, $I$:

$$I(P, T, X^{\mathrm{L}}) = I_0 \exp\left[\frac{-\Delta G(r_c(P, T, X^{\mathrm{L}}))}{k_b T}\right] \tag{4.4}$$

at which new crystals of the critical radius form, where $k_b$ is Boltzmann's constant. On average, half of these will rapidly dissolve, while the other half grow. The mean waiting time between nucleation events in a volume element in the F-layer, with volume $V(R)$, is

$$\tau(R, P, T, X^{\mathrm{L}}) = \frac{2}{I(P, T, X^{\mathrm{L}})V(R)}. \tag{4.5}$$

The expected nucleation rate and critical size for representative conditions are shown in Figure 6.

Classical nucleation theory, as illustrated by Figure 6, predicts a low probability of forming new solid particles in the F-layer by homogeneous nucleation, consistent with the findings of Shimizu et al. [60] who take this as support for a mush layer at the ICB. This is reminiscent of the "core nucleation paradox," where CNT predicts that the combination of the time, volume and undercooling available on Earth is insufficient to permit the inner core to form [58, 59, 61–63]. Our estimate of the nucleation rate, using free energy changes derived from the thermodynamic model, accords with previous estimates based on the available metallurgical data [58] and atomic scale simulation with [59], or without [61], substantial temperature extrapolation. There are two important difference between the situation for a two-component slurry and previous work considering the initial formation of the inner core. The first arises from the existence of a two-phase region in the phase diagram (Figure 2). This allows substantial undercooling below the liquidus to drive nucleation without resulting in a situation where all the undercooled liquid freezes once the first solid forms. The second difference is due to the use of a full thermodynamic model and the interplay between this and the depression of the liquidus by the addition of oxygen. In absolute terms (i.e. fixing the temperature and increasing the oxygen content of the liquid) adding oxygen dramatically decreases the nucleation rate because it lowers the free energy of the liquid (seen in the inset to Figure 6b). If instead we think in terms of undercooling below the liquidus, we find that nucleation rate is almost independent of oxygen content but that at fixed undercooling adding oxygen slightly increases the nucleation rate (shown in the main panel of Figure 6b). This is because the temperature dependence of $\Delta\mu_{\mathrm{Fe}}(P, T, X^{\mathrm{L}})$ is itself dependent on temperature and liquid composition [39]. This effect discounts any change in the composition of

the liquid caused by the nucleation event, and neither effects are significant enough to change the argument that nucleation from a homogeneous liquid is unlikely.

One resolution, which at least allows us to explore the behaviour of a slurry in the F-layer, is to appeal to heterogeneous nucleation where iron particles nucleate on some pre-existing solid. From geometrical arguments [57], a simple model of this process can be parameterised by $S(\theta)$ in Equation 4.1. The wetting angle for pre-existing oxides is expected to be $> 110^\circ$, while for metals it may be $< 25^\circ$ [58]. Figure 6c shows the effect of wetting angle on nucleation rate, with the homogeneous case reproduced for $\theta = 180^\circ$ and an enormous (100 order of magnitude) increase in nucleation rate with decreasing $\theta$ (i.e. for cases where the pre-existing solid is structurally and chemically similar to solid iron). At $\theta = 0^\circ$ the nucleation rate is entirely controlled by $I_0$, which is itself highly uncertain. For nucleation of the inner core, finding a source of these preexisting solid particles is difficult [58], but in the F-layer the inner core could conceivably act as a source of fragments of iron. Furthermore, once some solid forms it could fragment and act to multiply the number density of particles, as seen in recent tank experiments [64].

Given this state of uncertainty, we propose a relatively simple approach to handling nucleation in our model. We imagine the presence of some pervasive 'dust' in the F-layer providing abundant sites for heterogeneous nucleation. We set $\gamma = 1.08$ J m$^{-2}$ [59], $\theta = 5^\circ$ (appropriate for a metallic substrate), and treat $I_0$ as an adjustable parameter with which we can explore the behaviour of the slurry. Indeed, it turns out that the very rapid change in nucleation rate with $I_0$ allows us to tune the departure of the system from equilibrium and explore the ways a non-equilibrium slurry can behave. Incorporation of CNT as described above then means that the nucleation is turned off as the thermodynamic driving force decreases and increases with further departure from equilibrium.

## 5. A model of a slurry layer

The model developed in section 3 describes a single 'iron snow' particle falling through the F-layer, but it fails to capture several key aspects of the collective behaviour of iron particles and thus by itself is not capable of describing the F-layer as a whole. To make progress, we seek to build a simple model of the F-layer as a slurry. This model is designed to allow the consequences of the nucleation, growth and falling of the individual iron particles to be examined rather than to act as a definitive description of the F-layer. In order to construct this model we imagine that solid particles can nucleate anywhere within the two phase region before falling and growing until they ultimately settle on the inner core boundary contributing to inner core growth by sedimentation. As the particles grow they exclude light elements and thus act as a source of oxygen and latent heat allowing the temperature and composition of the layer to change. A self-consistent solution for the temperature and liquid composition within the layer requires coupling between the particle-scale model developed here and a continuum theory for the transfer of heat and mass through a two-phase slurry. However, the general continuum theory is complex, is reliant on poorly known interaction parameters and, despite recent progress [20, 65], is not fully developed for the two-component system. Therefore, in order to explore the possible behaviours of our model, we impose temperature and composition profiles inspired by previous equilibrium models [19] at the continuum scale. These profiles, shown in Figure 1 are tied to a constant composition and adiabatic temperature profile in the outer core above the F-layer such that the first intersection with the liquidus occurs 200 km above the ICB. This defines the F-layer region where a two-phase slurry can exist. The temperature and compositional profiles inside the F-layer follow second-order polynomials with zero derivative at the ICB (because we assume no direct freezing on the ICB) leaving one degree of freedom for each profile: the temperature and composition at the ICB, which are described by $\Delta T_{ICB}$ and $\Delta X_{ICB}$, respectively. In all cases we require the temperature in the F-layer to be below the liquidus for the imposed composition as this is required to provide the thermodynamic driving force for nucleation or growth. Because of the imposed temperature and composition we describe the model as "quasi-steady state" and note three important time-scales. We assume that changes to the solid-fraction in the layer

happen more slowly than the short time needed for individual particles to nucleate, fall and grow described above (which means we can form averages over the lifetime of many individual particles). However, evolution of the temperature and composition happens more slowly than changes in the solid-fraction, with the slowest timescale presumably controlled by secular cooling of the whole outer core.

We discretise the F-layer into $M$ radial layers of thickness $h = (R_f - R_{icb})/M$ and $N$ small equal area square patches which, at radius $R$, have area $A(R) = 4\pi R^2/N$. If $h \ll R$, the volume of an element is $V(R) = A(R)h$ and the horizontal spacing between the middle of adjacent volume elements is given by $s_h(R) = \sqrt{A(R)}$. We note that the model only requires explicit consideration of one column of elements because we assume spherical symmetry for the F-layer. Given the volume of each element and the temperature, pressure and composition of the liquid imposed we are able to evaluate the average time between nucleation events in each volume element from Equation 4.5. Assuming that the time needed for a particle to nucleate, fall, and grow is much shorter than the timescale of changes in the temperature and composition of the layer, we can examine the behaviour of average particles and note that, on average, nucleation events will take place at the centre of the volume element and particles regularly nucleate at these points at times $\tau$ seconds apart. The subsequent evolution of each particle as it grows, falls and ultimately impacts on the ICB is found by following the procedure described in section 3(c).

We describe the solid particles within the slurry in terms of their number density and size as functions of $R$. Our starting point is to calculate the vertical spacing between three particles nucleating in the same place in three consecutive nucleation events. These occur at time $t_0 - \tau$, $t_0$ and $t_0 + \tau$, all have initial radius $r_0$ (found from $r_c$ in Equation 4.2), and, apart from this difference in the initial condition, the three particles will follow the same trajectory to the ICB. This means we can use $R_p(t; R_0, r_0)$, the solution to the coupled ODEs (3.3) and (3.9) giving the time evolution of the particle nucleating at $R_0$, to find the vertical separation, $s_v$, between sequentially nucleating particles, given our ability to find $t(R_p)$ from the ODE solution:

$$s_v(R_p, R_0) = \frac{(R_p(t - \tau; R_0, r_0) - R_p(t; R_0, r_0)) + (R_p(t; R_0, r_0) - R_p(t + \tau; R_0, r_0))}{2}. \quad (5.1)$$

Here $s_v$ depends on both the location where the separation is measured (i.e. the particle location, $R_p$) and on the location where the particles nucleated ($R_0$). Equation 5.1 relies on our quasi-steady state assumption. At any location there can be multiple populations of particles, of different sizes that nucleated in different places, falling past each other. Each population is represented by the solution of coupled ODEs with different initial conditions.

Particles spread out in space as they grow and fall faster. Counteracting this tendency to spread out vertically as they fall, streams of particles nucleating in horizontally adjacent volume elements will tend to approach each other due to the spherical geometry of the F-layer. The *partial* particle number density, that is the contribution of the number of particles per unit volume at radius $R_p$ arising from particles which initially nucleated from a nucleation volume centred at $R_0$ ($R_p < R_0$), is then:

$$\bar{n}(R_p, R_0) = \frac{1}{s_v(R_p, R_0)s_h(R_p)^2}. \quad (5.2)$$

We can then find the total particle number density, $n(R_p)$, by summing up the partial particle densities from nucleation points above $R_p$:

$$n(R_p) = \sum_{R_0=R_p}^{R_F} \bar{n}(R_p, R_0). \quad (5.3)$$

Here, the summation runs over all of the possible nucleation locations ($R_0$) above the location where the number density is being evaluated ($R_p$) because particles only fall downwards. This means that if $R_p = R_{icb}$ there are $M$ terms in the summation and if $R_p$ is evaluated half way between the ICB and the top of the F-layer there are $M/2$ terms in the summation. Each term in the summation involves extracting results from solutions to the coupled ODEs with different

initial conditions. The solid volume fraction at a given position can be calculated in a similar way noting that the different particle populations will have different radii depending on where they nucleate

$$\phi(R_p) = \sum_{R_0 = R_p}^{R_F} \overline{n}(R_p, R_0) \frac{4}{3} \pi r_p(t(R_p); R_0, r_0)^3,$$ (5.4)

again the summation runs over each possible nucleation location above $R_p$, and the product is between the number density of particles nucleating at $R_0$ (in m$^{-3}$) and their volume (in m$^3$). The mass fraction of solid is found considering the densities of the two phases

$$\mathcal{M}(R_p) = \frac{\phi(R_p)\rho^S(R_p)}{\phi(R_p)\rho^S(R_p) + (1 - \phi(R_p))\rho^L(R_p)}.$$ (5.5)

Figure 7 shows the results of an example stratified F-layer with imposed temperature and compositional profiles illustrated in Figure 1 and material properties identical to those shown in light blue in Figure 5. The under-cooling, and thus driving force for nucleation and growth, increases with depth yielding an increasing nucleation rate and solid fraction from the top to the bottom of the F-layer. The inset histogram of particle size distribution as a function of radius shows that in all cases the particle population is dominated by a large number of very small particles. These are recently nucleated and have not yet grown enough to fall quickly, corresponding to the early parts of the trajectories shown in Figure 5(a). The largest particles in the population increase in radius downwards, reflecting the increased time available for growth of particles nucleating near the top of the layer, and the largest particles in the whole layer are found just above the ICB. These particles nucleated near the top of the layer and are the oldest particles as well as the largest and most rapidly falling. Maximum particle radii are smaller than the single particle cases described in section 3(c) because the under-cooling goes to zero at the top of the F-layer (so growth is slower).

The results of the model also give access to properties related to the thermal history of the Earth. These depend on the total growth rate of solid at a given radius within the F-layer. This Lagrangian derivative is found by finite difference of the particle radii

$$\dot{\phi}(R_p) = \frac{\mathrm{d}\phi(R_p)}{\mathrm{d}t} \approx \sum_{R_0 = R_p}^{R_F} \overline{n}(R_p, R_0) \frac{4\pi}{3} \frac{r_p(t(R_p) + \Delta t; R_0, r_0)^3 - r_p(t(R_p) - \Delta t; R_0, r_0)^3}{2\Delta t},$$ (5.6)

where the summation runs over each possible nucleation location above $R_p$ (see Equation 5.3). $\dot{\phi}(R_p)$ gives access to the rate of change of solid mass fraction

$$\dot{\mathcal{M}}(R_p) = \frac{\dot{\phi}(R_p)\rho^S(R_p)\rho^L(R_p)}{(\phi(R_p)\rho^S(R_p) + (1 - \phi(R_p))\rho^L(R_p))^2}.$$ (5.7)

Growth of solid results in the release of latent heat where the specific latent heat of crystallisation, $L$, is taken as 750 kJ kg$^{-1}$ [33]. Integrating over the F-layer gives the total heat production rate due to formation of solid in the layer, which we equate to the heat flux out of the layer because we assume fixed layer temperature:

$$Q^F = 4\pi \int_{R_{icb}}^{R_F} \dot{\mathcal{M}}(R)\rho^S(R)LR^2 \mathrm{d}R.$$ (5.8)

Finally, we calculate the rate of predicted inner core growth from sedimentation by evaluating the rate at which solid arrives at the ICB given its surface area:

$$G_{icb} = \frac{1}{4\pi R_{icb}^2} \int_{R_{icb}}^{R_F} \frac{I(R)}{2} \cdot \frac{4}{3} \pi r_p(R_{icb}; R, r_0)^3 \cdot 4\pi R^2 \mathrm{d}R$$ (5.9)
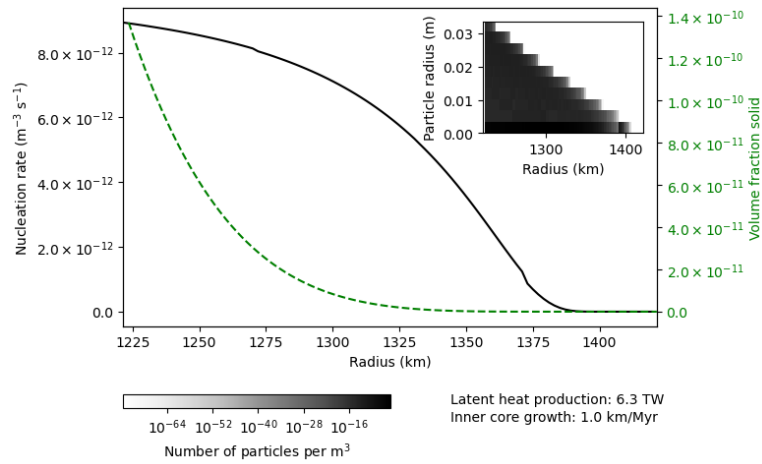
**Figure 7.** Key results from a slurry model of the F-layer with temperature and compositional profiles as shown in 1(c), $D^L = 1 \times 10^{-9}$ m$^2$ s$^{-1}$, $\nu^L = 2 \times 10^{-6}$ m$^2$/s (corresponding to the light blue square in in Figure 5) and $I_0 = 1 \times 10^{-11}$ s$^{-1}$ m$^{-3}$. The main panel shows the calculated nucleation rate (black) and volume fraction solid (green), which both increase downwards as the under-cooling increases. Nucleation starts close to $R = 1375$ km where the temperature profile drops sufficiently below the liquidus (see Figure 1), but the very low undercooling results in such small nucleation and growth rates that the volume fraction solid remains effectively zero until $R = 1275$ km where the under-cooling becomes much more significant. The inset histogram of the number density of particles of different sizes as a function of depth reveals that once particles start to grow they grow steadily with the largest particles found just above the ICB. However, small particles that have not yet grown enough to fall quickly continue to dominate the particle size distribution throughout the layer.

Equation 5.9 does not rely on the assumption of a quasi-steady state, only that all particles that nucleate reach the ICB on the timescale of inner core growth. Values for $Q^F$ and $G_{icb}$ calculated for our example simulation are given in Figure 7.

## 6. Plausible non-equilibrium models of the F-layer

We now search for model parameters that are consistent with geophysical observations, and outline the resulting model outputs for plausible F-layer configurations. For the Earth, our models must obey some important constraints. An inner core age in the range $0.5 - 1.5$ Gyrs gives mean growth rates in the range $0.8 - 2.4$ km Myr$^{-1}$ [33]. However, this estimate includes the effect of direct freezing at the interface, which is not accounted for in our model, and is therefore an upper bound on the allowed growth rate. The latent heat production is more tightly constrained for Earth as it cannot exceed the total heat $Q^c$ leaving the core. Estimates of $Q^c$ are usually in the range $5 - 17$ TW [1, 66] and unlikely to exceed $20$ TW [67]. However, given that secular cooling contributes at least $4$ TW [68], and more likely about $6$ TW [69], and gravitational energy another $2 - 4$ TW the latent heat contribution is expected to be around $6$ TW and no larger than $10$ TW [69]. We note that the the constraints on plausible values for $Q^F$ and $G_{icb}$ are not forced to be consistent as they are based on different observations that may relate to different time periods. However, we can estimate the latent heat released for a given inner core growth rate. $G_{icb}$ between $0.8$ and $2.4$ km Myr$^{-1}$ implies $Q^F$ between $4.5$ and $13.6$ TW, which is broadly consistent of the our independent estimate of $Q^F$. On the basis of these estimates, the combination of physical properties with thermal and compositional profiles shown in Figure 7 produces a 'viable' non-equilibrium model of a slurry with $Q^F$ and $G_{icb}$ within the expected range.

In Figure 8(a) we investigate the model behaviour by changing the imposed temperature or composition profiles, which are parameterised by $\Delta T_{ICB}$ and $\Delta X_{ICB}$ respectively (see Figure 1).
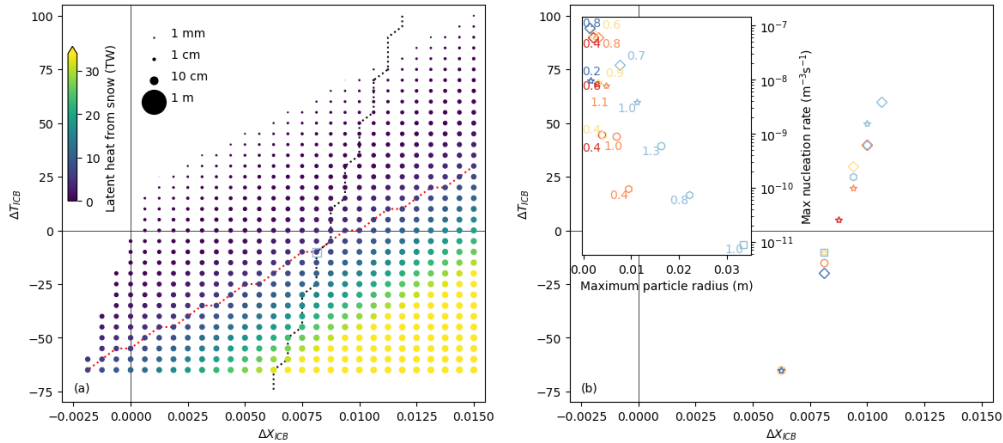
**Figure 8.** Gross properties of models of the F-layer. (a) Models with fixed material properties corresponding to the model shown in Figure 7 but with different thermal and compositional profiles as defined by $\Delta T_{ICB}$ and $\Delta X_{ICB}$ (See Figure 1). Symbol size represents the largest particle size and colour represents the latent heat released by the layer. The black dashed line connects model cases where the slurry is approximately 27.24 kg/m$^3$ denser than the extrapolated adiabat at the ICB and the red dashed line connects models releasing $\sim 6$ TW of latent heat. The model highlighted by a blue square is shown in Figure 7. (b) Locus of temperature and compositional profiles which result in successful models (27.24 kg/m$^3$ excess density and 6 TW of latent heat) for the different material properties. Symbol colours indicate $D^{\mathrm{L}}$ and $\nu^{\mathrm{L}}$ pairs (matching the colours used in Figure 5) and symbol shapes representing different nucleation pre-factors (diamonds: $I_0 = 1 \times 10^{-7}$; stars, $I_0 = 1 \times 10^{-8}$; circles, $I_0 = 1 \times 10^{-9}$; hexagons, $I_0 = 1 \times 10^{-10}$; squares, $I_0 = 1 \times 10^{-11}$ s$^{-1}$ m$^{-3}$). The inset shows the relationship between maximum particle radius and nucleation rate for these successful cases with the numerals indicating the inner core growth rate in km Myr$^{-1}$. Model inputs and outputs are tabulated in the supplementary information.

Here $\Delta T_{ICB}$ is the difference in temperature between an extrapolated adiabat (defined so as to intersect the liquidus at the top of the F-layer 200 km above the ICB) and the temperature at the ICB, while $\Delta X_{ICB}$ is the difference in composition between the well mixed convecting outer core (which always has 17 mol% oxygen) and the F-layer just above the ICB (negative values imply oxygen enrichment). We limit the parameter space by requiring that: 1) the temperature increases with depth in the F-layer, as suggested by previous models [6, 19] and is below the liquidus at the ICB as required for slurry solutions; 2) oxygen depletion at the ICB is at most 1.5% compared to the overlying outer core ($\Delta X_{ICB} \leq 0.015$) as suggested by the results of [19]; the liquid is stably stratified ($N_{BW}^2 < 0$). These constraints confine solutions to the region encompassed by points in Figure 8(a) with the upper boundary representing the liquidus and the left hand boundary representing the stability constraint. Stratified models can exist in regions where the liquid is enriched or depleted in oxygen compared to the overlying well-mixed outer core and in regions where the temperature is higher than or lower than the temperature of the adiabat projected to the ICB. Increasing the distance from equilibrium (increasing $\Delta X_{ICB}$ or decreasing $\Delta T_{ICB}$) drives larger $\dot{\mathcal{M}}$ from growth and nucleation leading to larger $r_p$ and higher $Q^F$. Both values are approximately constant along lines parallel to the liquidus (i.e. lines of constant $\Delta \mu_{\mathrm{Fe}}$). The maximum size of crystals saturates in the cm range because of the increased falling speed of large crystals discussed in section 3. The latent heat production increases exponentially with increasing $\Delta \mu_{\mathrm{Fe}}$ (the colour scale is saturated at Earth's surface heat flux), which is presumably driven by the nucleation rate.

Although Figure 8(a) shows a wide range of compositions and temperatures for an F-layer configuration where a slurry could exist, the range of models that are consistent with geophysical constraints on the present-day F-layer are more limited. We choose two particular observations

to winnow out Earth-like models from within the wedge of slurry models. First, we demand that the density difference between an outer core adiabat extrapolated to the ICB and the density of the slurry layer (including effects of temperature, composition, and solid fraction) matches the difference between PREM and AK135f such that models have an excess density of 27.24 kg/m$^3$. This essentially seismological constraint is represented by the black dashed line in Figure 8(a). In all such cases, we find a low amount of solid and that the excess density is predominantly caused the fact that $\Delta X_{ICB} > 0$. We also consider the heat produced by the layer. This must certainly be less than Earth's surface heat flux indicated by the yellow saturation in Figure 8(a), but as discussed above, is probably closer to 6 TW, the value indicated by the red dashed line. In Figure 8(a) these lines cross and we consider the model where these two constraints are met as 'Earth like' and it is that model that is shown in Figure 7. We emphasise that these choices are illustrative and do not capture the full range of possible 'Earth like' models where the excess density and latent heat production, as well as the composition and temperature of the overlying outer core could all differ from the models illustrated here.

Figure 8(b) shows the properties of 'Earth like' slurry solutions in $\Delta X_{ICB} - \Delta T_{ICB}$ space as a function of the nucleation pre-factor (shown as different symbol shapes), viscosity and oxygen diffusivity of the liquid (shown as different symbol colors). Changing these properties does not alter the density of the slurry (because the density difference is dominated by the density of the liquid, not the solid fraction which is always low) so successful models plot along a common line in $\Delta X_{ICB} - \Delta T_{ICB}$ space. Material properties that give higher solid production rates (e.g. caused by increasing the nucleation pre-factor or the diffusion coefficient) yield solutions that are closer to the liquidus at the ICB (smaller $\Delta \mu_{\text{Fe}}$, larger positive $\Delta T_{ICB}$) while properties that slow the solid production rate (e.g. decreasing the pre-factor or the diffusion rate) yield solutions that are further from the liquidus as they need larger $\Delta \mu_{\text{Fe}}$ (and thus negative $\Delta T_{ICB}$) to drive solid formation. The models have different maximum particle sizes, though all are dominated by a population of very small slowly falling particles, with the largest particles only reaching mm to cm sizes before they leave the layer. The predicted inner core growth rates ($0.4 - 1.3$ km Myr$^{-1}$) are below the maximum permitted growth rate assuming a young inner core growing at a constant rate. This is expected because we do not include direct freezing at the ICB and our growth rate estimates are therefore consistent with other geophysical inferences.

Overall, we find significant diversity of 'Earth like' slurry models of the F-layer where we don't need to carefully tune model parameters such as viscosity or light element diffusivity in order to match the expected heat production rate and density stratification for a low-volume fraction slurry. In contrast, we are unable to produce viable models assuming homogeneous nucleation of solid particles to form the slurry and do need to resort to alternative physical mechanisms where the nucleation rate effectively acts as a tuning parameter. In all cases excess Fe in the liquid ($0.6 - 1.06$ mol.% compared to the overlying well-mixed core) is the dominant direct cause of the density anomaly rather than the presence of solid particles. This is reassuring as it both accords with our assumption that the falling particles do not interact, and matches the predictions of previous equilibrium models. Indeed, our results yield much lower solid volume fractions ($1 \times 10^{-10} - 1 \times 10^{-11}$) than equilibrium models (e.g. $< 0.05$ [20]) as expected given that nucleation and growth must cease as the system approaches equilibrium. In terms of temperature, valid models can be sub- or super-adiabatic with the degree of under-cooling compared to the liquidus ($\approx 35 - 150$ K) required to drive crystal growth increasing as the intrinsic nucleation or growth rate decreases. This estimate of the undercooling required for nucleation complements previous independent inferences from mineralogical [61, 62] and geodynamic [70] modelling and is lower than the maximum undercooling allowed by the present-day thermal structure of the core [58, 71].

## 7. Conclusions

Our 'bottom up' construction of a model of a core slurry layer, focusing on processes that control the nucleation, growth and settling of isolated solid particles, has allowed us to explore the evolution of single particles in a two-phase system. One important feature of this approach is

that the temperature must depart from the liquidus temperature in order to allow the solid to form, something that is forbidden in equilibrium models. Building a quasi-steady state model of the whole slurry layer allows us to describe the number density, longevity and size distribution of particles within the layer. These properties are inaccessible (without additional assumption) in equilibrium models, which only predict the volume fraction solid. We have applied this model to the Earth's F-layer for a particular choice of Fe-O chemistry and varied the temperature and composition in the F-layer along with the intrinsic material properties of iron (the oxygen diffusivity, viscosity, and nucleation pre-factor). Even within this restricted model space we find a diversity of potential slurry models that are consistent with inferred properties of the F-layer and the heat budget of the core. In all cases, models are dominated by a large number of small slowly falling particles with a handful of the largest particles being limited to cm size. In common with equilibrium models the solid fraction is always small and it is the chemistry of the liquid that dominates the density structure of the layer.

One way to view our approach is as a framework to describe non-equilibrium processes that must operate in a core slurry layer. The framework incorporates micro-scale processes from fluid dynamics and mineral physics into a simple model of the whole slurry layer to probe core-scale processes that can be interrogated by seismology. The representation is designed to be flexible: alternative thermodynamic models containing different light elements can be used as long as the relevant chemical potentials are available, while different scaling laws for particle dynamics and parameterisations for nucleation and growth rate can be swapped for those chosen here. One caveat is our assumption that light elements do not enter the solid phase: lifting this assumption would be challenging because this would necessitate tracking the chemistry of the solid particles as they fall. Nevertheless, the model framework is sufficiently general that it could be readily adapted to represent snow zones in other terrestrial planetary cores.

Immediate extensions to our work include the need to compare outputs with a wider range of geophysical observations and consider different outer core adiabats and chemistries, as well as including the possibility of some direct freezing on the inner core. This would imply the need to alter the temperature and compositional profile imposed on the F-layer to capture the release of latent heat and light elements associated with direct freezing. Including direct freezing would also alter the growth and nucleation rate of solid particles within the slurry layer. It is also desirable to produce solutions where the temperature and composition are not imposed, but solved self-consistently. This could be achieved by coupling our particle-based framework to a continuum model of two-component non-equilibrium slurry dynamics. However, this is non-trivial as it would be necessary to capture the heat and chemical fluxes through the layer and, in a slurry, there is a necessary advection of heat and chemical components by fluid flow and this fluid flow would impact the falling velocity of the particles. We imagine that such an approach would necessitate using velocities and densities of the falling particles to evaluate the velocity of fluid flow before iterating to find particle falling velocities and growth rates that are consistent with the resulting fluid flow. Eventually this should result in a model where the temperature, composition, particle density and particle falling rates are all consistent with each other. Our expectation is that such an exercise would require significant work to make the coupled model theoretically and practically viable.

# References

1 Nimmo F. 2015 Energetics of the core. *Treatise on geophysics* **8**, 27–55.
2 Bergman MI. 1997 Measurements of electric anisotropy due to solidification texturing and the implications for the Earth's inner core. *Nature* **389**, 60–63.

3  Alboussiere T, Deguen R, Melzani M. 2010 Melting-induced stratification above the Earth's inner core due to convective translation. *Nature* **466**, 744–747.

4  Deguen R, Olson P, Reynolds E. 2014 F-layer formation in the outer core with asymmetric inner core growth. *Comptes Rendus Geoscience* **346**, 101–109.

5  Deguen R, Alboussière T, Labrosse S. 2018 Double-diffusive translation of Earth's inner core. *Geophysical Journal International* **214**, 88–107.

6  Gubbins D, Masters G, Nimmo F. 2008 A thermochemical boundary layer at the base of Earth's outer core and independent estimate of core heat flux. *Geophysical Journal International* **174**, 1007–1018.

7  Wong J, Davies CJ, Jones CA. 2018 A Boussinesq slurry model of the F-layer at the base of Earth's outer core. *Geophysical Journal International* **214**, 2236–2249.

8  Hauck SA, Aurnou JM, Dombard AJ. 2006 Sulfur's impact on core evolution and magnetic field generation on Ganymede. *Journal of Geophysical Research* **111**, E09008.

9  Stewart AJ, Schmidt MW, van Westrenen W, Liebske C. 2007 Mars: A New Core-Crystallization Regime. *Science* **316**, 1323–1325.

10  Rückriemen T, Breuer D, Spohn T. 2015 The Fe snow regime in Ganymede's core: A deep-seated dynamo below a stable snow zone: FE-SNOW IN GANYMEDE'S CORE. *Journal of Geophysical Research: Planets* **120**, 1095–1118.

11  Dumberry M, Rivoldini A. 2015 Mercury's inner core size and core-crystallization regime. *Icarus* **248**, 254–268.

12  Davies CJ, Pommier A. 2018 Iron snow in the Martian core?. *Earth and Planetary Science Letters* **481**, 189–200.

13  Edgington A, Vočadlo L, Stixrude L, Wood I, Dobson D, Holmström E. 2019 The top-down crystallisation of Mercury's core. *Earth and Planetary Science Letters* **528**, 115838.

14  Williams Q. 2009 Bottom-up versus top-down solidification of the cores of small solar system bodies: Constraints on paradoxical cores. *Earth and Planetary Science Letters* **284**, 564–569.

15  Loper DE, Roberts PH. 1981 A STUDY OF CONDITIONS AT THE INNER CORE BOUNDARY OF THE EARTH. *Physics of the Earth and Planetary Interiors* **24**, 302 – 307.

16  Loper DE, Roberts PH. 1987 Boussinesq model of a slurry. In Loper DE, editor, *Structure and Dynamics of partially solidified systems* NATO Advanced Sciences Institute Series E: Applied Sciences pp. 293 – 322. Martinus Nijhoff.

17  Loper DE, Roberts PH. 1977 On the motion of an iron-alloy core containing a slurry: I. general theory. *Geophysical & Astrophysical Fluid Dynamics* **9**, 289 – 321.

18  Zhang Y, Nelson P, Dygert N, Lin JF. 2019 Fe alloy slurry and a compacting cumulate pile across Earth's inner-core boundary. *Journal of Geophysical Research: Solid Earth* **124**, 10954–10967.

19  Wong J, Davies CJ, Jones CA. 2021 A regime diagram for the slurry F-layer at the base of Earth's outer core. *Earth and Planetary Science Letters* **560**, 116791.

20  Wilczyński F, Davies CJ, Jones CA. 2023 A two-phase pure slurry model for planetary cores: one-dimensional solutions and implications for Earth's F-layer. *Journal of Fluid Mechanics* **976**, A5.

21  Song X, Helmberger DV. 1992 Velocity structure near the inner core boundary from waveform modeling. *Journal of Geophysical Research: Solid Earth* **97**, 6573–6586.

22  Kennett BL, Engdahl E, Buland R. 1995 Constraints on seismic velocities in the Earth from traveltimes. *Geophysical Journal International* **122**, 108–124.

23  Souriau A, Poupinet G. 1991 The velocity profile at the base of the liquid core from PKP(BC+Cdiff) data: An argument in favour of radial inhomogeneity. *Geophysical Research Letters* **18**, 2023–2026.

24  Souriau A, Roudil P. 1995 Attenuation in the uppermost inner core from broad-band GEOSCOPE PKP data. *Geophysical Journal International* **123**, 572–587.

25  Song X, Helmberger D. 1995 A *P* wave model of Earth's core. *Journal of Geophysical Research: Solid Earth* **100**, 9817–9830.

26  Zou Z, Koper KD, Cormier VF. 2008 The structure of the base of the outer core inferred from seismic waves diffracted around the inner core. *Journal of Geophysical Research* **113**, B05314.

27 Ohtaki T, Kaneshima S. 2015 Independent estimate of velocity structure of Earth's lowermost outer core beneath the northeast Pacific from PKiKP – PKPbc differential traveltime and dispersion in PKPbc: INDEPENDENT ESTIMATE OF *F* LAYER VELOCITY. *Journal of Geophysical Research: Solid Earth* **120**, 7572–7586.

28 Souriau A, Calvet M. 2015 Deep Earth Structure: the Earth's cores. In *Treatise on Geophysics* vol. 1 pp. 725–757. Elsevier.

29 Dziewonski AM, Anderson DL. 1981 Preliminary reference Earth model. *Physics of the Earth and Planetary Interiors* **25**, 297 – 356.

30 Gubbins D, Masters G, Nimmo F. 2008 A thermochemical boundary layer at the base of Earth's outer core and independent estimate of core heat flux. *Geophysical Journal International* **174**, 1007–1018.

31 Pozzo M, Davies CJ, Alfè D. 2022 Towards reconciling experimental and computational determinations of Earth's core thermal conductivity. *Earth and Planetary Science Letters* **584**, 117466.

32 Frost D, Lasbleis M, Chandler B, Romanowicz B. 2021 Dynamic history of the inner core constrained by seismic anisotropy. *Nature Geoscience* **14**, 531–535.

33 Davies C, Pozzo M, Gubbins D, Alfè D. 2015 Constraints from material properties on the dynamics and evolution of Earth's core. *Nature Geoscience* **8**, 678–685.

34 Gubbins D, Sreenivasan B, Mound J, Rost S. 2011 Melting of the Earth's inner core. *Nature* **473**, 361–363.

35 Solomatov VS, Stevenson DJ. 1993 Kinetics of crystal growth in a terrestrial magma ocean. *Journal of Geophysical Research: Planets* **98**, 5407–5418.

36 Loper DE. 1992 A nonequilibrium theory of a slurry. *Continuum Mechanics and Thermodynamics* **4**, 213 – 245.

37 Alfè D, Gillan MJ, Price GD. 2002 Complementary approaches to the *ab initio* calculation of melting properties. *Journal of Chemical Physics* **116**, 6170 – 6177.

38 Alfè D, Gillan M, Price G. 2007 Temperature and composition of the Earth's core. *Contemporary Physics* **48**, 63–80.

39 Komabayashi T. 2014 Thermodynamics of melting relations in the system Fe-FeO at high pressure: Implications for oxygen in the Earth's core. *Journal of Geophysical Research: Solid Earth* **119**, 4164–4177.

40 Etter M, Dinnebier RE. 2014 Direct parameterization of the pressure-dependent volume by using an inverted approximate Vinet equation of state. *Journal of Applied Crystallography* **47**, 384–390.

41 Rückriemen T, Breuer D, Spohn T. 2018 Top-down freezing in a Fe–FeS core and Ganymede's present-day magnetic field. *Icarus* **307**, 172–196.

42 Pozzo M, Davies C, Gubbins D, Alfè D. 2013 Transport properties for liquid silicon-oxygen-iron mixtures at Earth's core conditions. *Physical Review B* **87**, 014110.

43 Clift R, Gauvin W. 1970 The motion of particles in turbulent gas streams. In *Chemeca 70: A conference convened by the Australian National Committee of the Institution of Chemical Engineers and the Australian Academy of Science* pp. 14–28. Butterworths and the Institution of Chemical Engineers [Chatswood, N.S.W.].

44 Clift R, Gauvin W. 1971 Motion of entrained particles in gas streams. *The Canadian Journal of Chemical Engineering* **49**, 439–448.

45 Zhang Y, Xu Z. 2003 Kinetics of convective crystal dissolution and melting, with applications to methane hydrate dissolution and dissociation in seawater. *Earth and Planetary Science Letters* **213**, 133–148.

46 Inman BG, Davies CJ, Torres CR, Franks PJS. 2020 Deformation of ambient chemical gradients by sinking spheres. *Journal of Fluid Mechanics* **892**, A33.

47 Grossmann S, Lohse D. 2000 Scaling in thermal convection: a unifying theory. *Journal of Fluid Mechanics* **407**, 27–56.

48 Dziewonski AM, Anderson DL Preliminary Reference Earth Model. **25**, 297–356.

49 Montagner JP, Kennett BLN How to Reconcile Body-Wave and Normal-Mode Reference Earth Models. **125**, 229–248.

50 Wilson HW. 1900 On the velocity of solidification and viscosity of super-cooled liquids. *Philosophical Magazine* **50**, 238–250.

51 Frenkel J. 1946 *Kinetic Theory of Liquids*. Oxford University Press.

52 Coriell S, Turnbull D. 1982 Relative roles of heat transport and interface rearrangement rates in the rapid growth of crystals in undercooled melts. *Acta Metallurgica* **30**, 2135–2139.

53 Mikheev L, Chernov A. 1991 Mobility of a diffuse simple crystal—melt interface. *Journal of Crystal Growth* **112**, 591–596.

54 Sun G, Xu J, Harrowell P. 2018 The mechanism of the ultrafast crystal growth of pure metals from their melts. *Nature Materials* **17**, 881–886.

55 Shampine LF. 1986 Some practical {R}unge-{K}utta formulas. *Mathematics of Computation* **46**, 135 – 150.

56 Virtanen P, Gommers R, Oliphant TE, Haberland M, Reddy T, Cournapeau D, Burovski E, Peterson P, Weckesser W, Bright J, van der Walt SJ, Brett M, Wilson J, Millman KJ, Mayorov N, Nelson ARJ, Jones E, Kern R, Larson E, Carey CJ, Polat I, Feng Y, Moore EW, VanderPlas J, Laxalde D, Perktold J, Cimrman R, Henriksen I, Quintero EA, Harris CR, Archibald AM, Ribeiro AH, Pedregosa F, van Mulbregt P, SciPy 1.0 Contributors, Vijaykumar A, Bardelli AP, Rothberg A, Hilboll A, Kloeckner A, Scopatz A, Lee A, Rokem A, Woods CN, Fulton C, Masson C, H\"aggstr\"om C, Fitzgerald C, Nicholson DA, Hagen DR, Pasechnik DV, Olivetti E, Martin E, Wieser E, Silva F, Lenders F, Wilhelm F, Young G, Price GA, Ingold GL, Allen GE, Lee GR, Audren H, Probst I, Dietrich JP, Silterra J, Webber JT, Slavi\vc J, Nothman J, Buchner J, Kulick J, Sch\"onberger JL, de Miranda Cardoso JV, Reimer J, Harrington J, Rodríguez JLC, Nunez-Iglesias J, Kuczynski J, Tritz K, Thoma M, Newville M, K\"ummerer M, Bolingbroke M, Tartre M, Pak M, Smith NJ, Nowaczyk N, Shebanov N, Pavlyk O, Brodtkorb PA, Lee P, McGibbon RT, Feldbauer R, Lewis S, Tygier S, Sievert S, Vigna S, Peterson S, More S, Pudlik T, Oshima T, Pingel TJ, Robitaille TP, Spura T, Jones TR, Cera T, Leslie T, Zito T, Krauss T, Upadhyay U, Halchenko YO, V\'azquez-Baeza Y. 2020 SciPy 1.0: fundamental algorithms for scientific computing in Python. *Nature Methods* **17**, 261–272.

57 Christian JW. 2002 *The Theory of Transformations in Metals and Alloys*. Oxford: Pergamon Press.

58 Huguet L, Van Orman JA, Hauck SA, Willard MA. 2018 Earth's inner core nucleation paradox. *Earth and Planetary Science Letters* **487**, 9–20.

59 Davies CJ, Pozzo M, Alfè D. 2019 Assessing the inner core nucleation paradox with atomic-scale simulations. *Earth and Planetary Science Letters* **507**, 1 – 9.

60 Shimizu H, Poirier J, Le Mouël J. 2005 On crystallization at the inner core boundary. *Physics of the Earth and Planetary Interiors* **151**, 37–51.

61 Wilson AJ, Walker AM, Alfè D, Davies CJ. 2021 Probing the nucleation of iron in Earth's core using molecular dynamics simulations of supercooled liquids. *Physical Review B* **103**, 214113.

62 Sun Y, Zhang F, Mendelev MI, Wentzcovitch RM, Ho KM. 2022 Two-step nucleation of the Earth's inner core. *Proceedings of the National Academy of Sciences* **119**, e2113059119.

63 Alfred W, Andrew W, Dario A, Christopher D. 2023 Can homogeneous nucleation resolve the inner core nucleation paradox?. *Earth and Planetary Science Letters* **000**, 000–000.

64 Huguet L, Le Bars M, Deguen R. 2023 A laboratory model for iron snow in planetary cores. *Geophysical Research Letters* **50**, e2023GL105697.

65 Bercovici D, Mulyukova E. 2020 Two-phase magnetohydrodynamics: Theory and applications to planetesimal cores. *Physics of the Earth and Planetary Interiors* **300**, 106432.

66 Jaupart C, Labrosse S, Lucazeau F, Mareschal JC. 2015 Temperatures, Heat, and Energy in the Mantle of the Earth. In *Treatise on Geophysics Geophysics*. Elsevier B. V. Section: 7.06.

67 Frost DA, Avery MS, Buffett BA, Chidester BA, Deng J, Dorfman SM, Li Z, Liu L, Lv M, Martin JF. 2022 Multidisciplinary constraints on the thermal-chemical boundary between Earth's core and mantle. *Geochemistry, Geophysics, Geosystems* **23**, e2021GC009764.

68 Gubbins D, Alfè D, Masters G, Price GD, Gillan M. 2004 Gross thermodynamics of two-component core convection. *Geophysical Journal International* **157**, 1407 – 1414.

69 Davies CJ. 2015 Cooling history of Earth's core with high thermal conductivity. *Physics of the Earth and Planetary Interiors* **247**, 65 – 79.

70  Lasbleis M, Kervazo M, Choblet G. 2020 The fate of liquids trapped during the Earth's inner core growth. *Geophysical Research Letters* **47**, e2019GL085654.

71  Wilson AJ, Alfè D, Walker AM, Davies CJ. 2023 Can homogeneous nucleation resolve the inner core nucleation paradox?. *Earth and Planetary Science Letters* **614**, 118176.

# Supplementary Information for "A non-equilibrium slurry model for planetary cores with application to Earth's F-layer"

A. M. Walker, C. J. Davies, A. J. Wilson and M. I. Bergman

February 2024

This document consists of:

- A table of symbols and values used to define the model presented in the main text.

- A derivation of the boundary condition on a falling particle that relates the compositional gradient at the particle-liquid interface to the particle growth rate (equation 3.9 of the main text).

- A table reporting key results of the 'Earth like' models summarised in Figure 8(b) in the main text.

This supplementary information is accompanied by the software that produces the model output presented in the main text. This is available at:

https://zenodo.org/doi/10.5281/zenodo.12684127

and allows all model instances to be run, and figures shown in main text to be produced.

| Symbol | Units | Meaning | First Use | Value |
|---|---|---|---|---|
| $t$ | s | Time | Eq. 3.3 | |
| $k_b$ | J K$^{-1}$ | Boltzmann constant | Eq. 4.4 | |
| $R_g$ | J mol$^{-1}$ | Gas constant | Eq. 2.1 | |
| $R$ | m | Radial distance from centre of planet | Fig. 1 | |
| $R_F$ | km | Radius of the top of the F-layer | Eq. 5.4 | 1421 |
| $R_{ICB}$ | km | Radius of the inner core boundary | Eq. 5.4 | 1221 |
| $R_p$ | m | Position of a particle | Fig. 1 | |
| $R_0$ | m | Initial position of particle | Eq. 5.1 | |
| $r$ | m | Distance from centre of particle | Fig 1. | |
| $r_p$ | m | Particle radius | Fig 1. | |
| $r_c$ | m | Critical radius | Eq. 4.2 | |
| $r_0$ | m | Initial radius of particle | Eq. 5.1 | |
| $T$ | K | Temperature | Eq. 2.1 | |
| $P$ | GPa | Pressure | Eq. 2.1 | |
| $X^L$ | | Liquid composition (mole fraction Fe; 1.0 is pure Fe, 0.0 is pure FeO) | Eq. 2.1 | |
| $X^S$ | | Solid composition (mole fraction Fe) | Eq. 2.1 | |
| $\rho^L$ | kg m$^{-3}$ | Liquid Density | Eq. 3.1 | |
| $\rho^S$ | kg m$^{-3}$ | Solid Density | Eq. 3.3 | |
| $\mu_{\text{Fe}}^{ph}$ | J mol$^{-1}$ | Chemical potential of iron in solid ($ph = $ S) or liquid ($ph = $ L) phase | Eq. 2.1 | |
| $\Delta\mu_{\text{Fe}}$ | J mol$^{-1}$ | Chemical potential difference iron in solid and liquid phase | Eq. 2.1 | |
| $X^{tot}$ | | Bulk composition (mole fraction Fe) | Eq. 2.2 | |
| $\mathcal{X}$ | | Solid fraction by mole | Eq. 2.2 | |
| $\phi$ | | Solid fraction by volume | Eq. 5.4 | |
| $\mathcal{M}$ | | Solid fraction by mass | Eq. 5.5 | |
| $\dot{\phi}$ | $s^{-1}$ | Rate of change of solid fraction by volume | Eq. 5.6 | |
| $\dot{\mathcal{M}}$ | $s^{-1}$ | Rate of change of solid fraction by mass | Eq. 5.7 | |
| $Re$ | | Reynolds number | Eq. 3.1 | |
| $Sc$ | | Schmidt Number | Eq. 3.4 | |
| $Pe_C$ | | Compositional Péclet Number | Eq. 3.4 | |
| $Fr$ | | Froude Number | Eq. 3.4 | |
| $w_p$ | m s$^{-1}$ | Particle falling velocity | Eq. 3.1 | |
| $C_D$ | | Drag coefficient | Eq. 3.2 | |
| $N_{BV}$ | $s^{-1}$ | Brunt–Väisälä Frequency | Eq. 3.4 | |
| $\rho'$ | kg m$^{-3}$ | Density deviation from well-mixed state | Eq. 3.5 | |
| $\delta C$ | m | Chemical boundary layer thickness | Eq. 3.6 | |
| $k_0$ | m s$^{-1}$ | Growth rate prefactor | Eq. 3.8 | |
| $\Delta G$ | J | Energy change of nucleation | Eq. 4.1 | |

| Symbol | Units | Description | Eq. | Value | |
|---|---|---|---|---|---|
| $g_{sl}$ | J m$^{-3}$ | Free energy difference between solid and liquid | Eq. 4.1 | | |
| $\gamma$ | J m$^{-2}$ | Surface energy | Eq. 4.1 | 1.08 | |
| $\theta$ | $^{\circ}$ | Wetting angle | Eq. 4.1 | 5 | |
| $I$ | s$^{-1}$ m$^{-3}$ | Nucleation rate | Eq. 4.4 | | |
| $I_0$ | s$^{-1}$ m$^{-3}$ | Nucleation prefactor | Eq. 4.4 | | |
| $\tau$ | s m$^3$ | Nucleation waiting time | Eq. 4.5 | | |
| $s_v$ | m | Vertical separation of particles | Eq. 5.1 | | |
| $s_h$ | m | Horizontal separation of particles | Eq. 5.1 | | |
| $\bar{n}$ | m$^{-3}$ | Partial number density of particles | Eq. 5.2 | | |
| $n$ | m$^{-3}$ | Total number density of particles | Eq. 5.3 | | |
| $G_{icb}$ | m s$^{-1}$ | Inner Core Growth Rate | Eq. 5.7 | | |
| $g$ | m$^2$ s$^{-1}$ | Gravitational acceleration | Eq. 3.3 | 4.4 | |
| $\nu^{\mathrm{L}}$ | m$^2$ s$^{-1}$ | Kinematic viscosity of liquid | Eq. 3.1 | $10^{-5}$ $10^{-18}$ | – |
| $D^{\mathrm{L}}$ | m$^2$ s$^{-1}$ | Oxygen diffusion coefficient | Eq. 3.4 | $10^{-9}$ $10^{-12}$ | – |

Table 1: Symbols and values used to define the model presented in the main text. Where appropriate units and first appearance are listed.

# Chemical Boundary Condition on a Falling Solid Particle

In the following we will work exclusively in spherical coordinates and all variables will depend only on the radial coordinate $r$ with origin at the particle centre. All concentrations are weight fractions. Subscripts $s$ and $l$ denote the solid and liquid phases respectively.

Consider a single stationary and isolated particle at pressure $P$ and temperature $T$. At each radius pressure, temperature and composition far from a particle are assumed to be constant and denoted by $P_0$, $T_0$ and $c_0$ respectively ($c$ is the mass fraction oxygen). We neglect fluctuations in $P$ near the solid-liquid interface, which are expected to be small [1]. We also assume that particles reach thermal equilibrium much faster than chemical equilibrium: for a 1 mm radius particle the thermal diffusion time $\tau_D = r_p^2/\kappa \sim 1$ s, which is much faster than any other timescale in our model. We therefore set $P = P_0$ and $T = T_0$ everywhere.

The chemical boundary condition at the moving particle-fluid interface can be obtained by considering mass conservation of oxygen at the mutual interface. This equation can be written generally for both solid and liquid phases and is given by

$$\rho_i \frac{\partial c_i}{\partial t} + \rho_i (\mathbf{v}_i \cdot \nabla) c_i + \nabla \cdot \mathbf{i}_i = 0, \tag{1}$$

where $i \in \{s, l\}$, $\mathbf{v}_i$ is the velocity, and $\mathbf{i}_i$ is the mass flux of O, defined below. This equation can be rewritten as

$$\frac{\partial \rho_i c_i}{\partial t} + \nabla \cdot (\rho_i \mathbf{v}_i c_i) + \nabla \cdot \mathbf{i}_i = 0, \tag{2}$$

which satisfies conservation of total mass,

$$\frac{\partial \rho_i}{\partial t} + \nabla \cdot (\rho_i \mathbf{v}_i) = 0. \tag{3}$$

We now integrate equation (2) over a pill-box of volume $V$ and surface $A$ straddling the surface of the moving particle using the Leibniz relation

$$\int \frac{\partial X}{\partial t} \, \mathrm{d}V = \frac{\mathrm{d}}{\mathrm{d}t} \left( \int X \mathrm{d}V \right) - \oint X \mathbf{U} \cdot \mathrm{d}\mathbf{A}, \tag{4}$$

for an arbitrary quantity $X$, where $\mathbf{U}$ is the interface velocity, to obtain

$$\frac{\mathrm{d}}{\mathrm{d}t} \left( \int \rho_i c_i \mathrm{d}V \right) - \oint \rho_i c_i \mathbf{U} \cdot \mathrm{d}\mathbf{A} + \oint \rho_i c_i \mathbf{v}_i \cdot \mathrm{d}\mathbf{A} + \oint \mathbf{i}_i \cdot \mathrm{d}\mathbf{A} = 0. \tag{5}$$

Performing the standard pillbox analysis, the first term on the LHS becomes a point source of mass, which is ignored. The result is:

$$\oint \mathbf{i}_i \cdot \mathrm{d}\mathbf{A} = \oint \rho_i c_i (\mathbf{U} - \mathbf{v}_i) \cdot \mathrm{d}\mathbf{A}. \tag{6}$$

The surface integrals have two terms, one on the liquid side and one on the solid side. We define $\mathbf{n}$ as the unit vector pointing radially outwards from the particle and note that $\mathrm{d}\mathbf{A} = \mathbf{n}\mathrm{d}A$ on the upper (liquid-side) surface and $\mathrm{d}\mathbf{A} = -\mathbf{n}\mathrm{d}A$ on the lower surface. For spherical particles we also have $\oint \mathbf{i}_i \cdot \mathrm{d}\mathbf{A} = 4\pi r_p^2 \mathbf{i}_i \cdot \mathrm{d}\mathbf{A}$. Denoting $\langle X \rangle = X_l - X_s$ we have

$$\langle \mathbf{i} \cdot \mathbf{n} \rangle = \langle \rho c \rangle \left( \mathbf{U} - \mathbf{v} \right) \cdot \mathbf{n}. \tag{7}$$

We assume that no O enters the solid ($\mathbf{i}_s = 0$) and a no-penetration condition on the fluid at the interface ($\mathbf{v} = 0$), the latter being consistent with the boundary conditions imposed by [2] (their equation 2.13). Denoting $\mathbf{U} \cdot \mathbf{n} = \mathrm{d}r/\mathrm{d}t$ and $\mathbf{i} \cdot \mathbf{n} = i_l$ we finally obtain

$$i_l = \rho_l c_l \frac{\mathrm{d}r}{\mathrm{d}t}, \tag{8}$$

which is equation 19 in [3]. The flux $\mathbf{i}_l$ is given by

$$i_l = -\rho_l D_l \frac{\partial c_l}{\partial r}, \tag{9}$$

and so

$$\frac{\partial c_l}{\partial r} = -\frac{c_l}{D_l} \frac{\mathrm{d}r}{\mathrm{d}t}. \tag{10}$$

In this case a positive growth rate corresponds to a positive flux of O away from the sphere surface ($\mathbf{n}$ is defined positive outwards). Note that [2] impose zero flux on the sphere surface in their calculations. In the main text we work in terms of mole fraction iron in the liquid (to correspond to the definition of the thermodynamic model) rather than the mass fraction of oxygen (used here so as to correspond to the fluid dynamics literature). This results in a sign change between Equation 10 and Equation 3.9 in the main text.

| $D^L$ | $\eta^L$ | $I_0$ | $\Delta T_{ICB}$ | $\Delta X_{ICB}$ | $Q^F$ | $\Delta\rho$ | $G_{ICB}$ | $\max r_p$ | $\max I$ | $\max\phi$ | Symbol |
|---|---|---|---|---|---|---|---|---|---|---|---|
| 1e-11 | 3e-05 | 1e-11 | – | – | – | – | – | – | – | – | red square |
| 1e-11 | 3e-05 | 1e-07 | 40 | 0.01 | 7.13 | 27.6 | 0.377 | 0.00201 | 6.1e-08 | 2.85e-09 | red diamond |
| 1e-11 | 3e-05 | 1e-09 | -65 | 0.00625 | 3.1 | 26.3 | 0.364 | 0.00392 | 9.56e-10 | 6.78e-10 | red circle |
| 1e-11 | 3e-05 | 1e-10 | – | – | – | – | – | – | – | – | red hexagon |
| 1e-11 | 3e-05 | 1e-08 | 5 | 0.00875 | 6.66 | 27.2 | 0.632 | 0.0029 | 8.55e-09 | 2.14e-09 | red star |
| 6e-08 | 6e-08 | 1e-11 | – | – | – | – | – | – | – | – | orange square |
| 1e-11 | 6e-08 | 1e-07 | 40 | 0.01 | 5 | 27.6 | 0.834 | 0.00313 | 6.1e-08 | 3.77e-10 | orange diamond |
| 1e-11 | 6e-08 | 1e-09 | -15 | 0.00813 | 6.17 | 27.2 | 0.987 | 0.00695 | 9.05e-10 | 3.12e-10 | orange circle |
| 1e-11 | 6e-08 | 1e-10 | -65 | 0.00625 | 2.5 | 26.3 | 0.398 | 0.00941 | 9.56e-11 | 1.09e-10 | orange hexagon |
| 1e-11 | 6e-08 | 1e-08 | 20 | 0.00937 | 6.9 | 27.6 | 1.12 | 0.00474 | 7.92e-09 | 4.21e-10 | orange star |
| 1e-11 | 2e-06 | 1e-11 | – | – | – | – | – | – | – | – | yellow square |
| 1e-11 | 2e-06 | 1e-07 | 30 | 0.00937 | 4.82 | 26.6 | 0.608 | 0.00205 | 7.02e-08 | 7.5e-10 | yellow diamond |
| 1e-11 | 2e-06 | 1e-09 | -65 | 0.00625 | 2.39 | 26.3 | 0.363 | 0.00408 | 9.56e-10 | 2.02e-10 | yellow circle |
| 1e-11 | 2e-06 | 1e-10 | – | – | – | – | – | – | – | – | yellow hexagon |
| 1e-11 | 2e-06 | 1e-08 | -10 | 0.00813 | 6.24 | 26.7 | 0.919 | 0.00307 | 8.93e-09 | 6.89e-10 | yellow star |
| 1e-09 | 2e-06 | 1e-11 | -10 | 0.00813 | 6.28 | 26.7 | 1.01 | 0.0335 | 8.93e-12 | 1.37e-10 | light blue square |
| 1e-09 | 2e-06 | 1e-07 | 60 | 0.0106 | 4.42 | 27.6 | 0.699 | 0.0076 | 1.87e-08 | 2.23e-10 | light blue diamond |
| 1e-09 | 2e-06 | 1e-09 | 40 | 0.01 | 7.59 | 27.6 | 1.25 | 0.0162 | 6.1e-10 | 2.62e-10 | light blue circle |
| 1e-09 | 2e-06 | 1e-10 | 25 | 0.00937 | 5.17 | 27.1 | 0.843 | 0.0221 | 7.53e-11 | 1.45e-10 | light blue hexagon |
| 1e-09 | 2e-06 | 1e-08 | 50 | 0.01 | 6.19 | 26.6 | 1.02 | 0.0111 | 3.9e-09 | 2.71e-10 | light blue star |
| 1e-12 | 2e-06 | 1e-11 | – | – | – | – | – | – | – | – | dark blue square |
| 1e-12 | 2e-06 | 1e-07 | -20 | 0.00813 | 6.35 | 27.7 | 0.833 | 0.00127 | 9.15e-08 | 1.58e-09 | dark blue diamond |
| 1e-12 | 2e-06 | 1e-09 | – | – | – | – | – | – | – | – | dark blue circle |
| 1e-12 | 2e-06 | 1e-10 | – | – | – | – | – | – | – | – | dark blue hexagon |
| 1e-12 | 2e-06 | 1e-08 | -65 | 0.00625 | 1.43 | 26.3 | 0.197 | 0.0015 | 9.56e-09 | 2.95e-10 | dark blue star |

Table 2: Input parameters and key results for the 'Earth like' models shown in Figure 8b of the main text. $\Delta T_{ICB}$ and $\Delta X_{ICB}$ are the values which result in the closest match to $Q^F$ and $\Delta\rho$ given the grid spacing used in the search. Maximum particle size, nucleation rate and volume fraction solid inevitably occurs at the base of the layer. Units are as reported in Table 1, above.

# References

[1] D. E. Loper and P. H. Roberts. Boussinesq model of a slurry. In D. E. Loper, editor, *Structure and Dynamics of Partially Solidified Systems*, NATO Advanced Sciences Institute Series E: Applied Sciences, pages 293–322. Martinus Nijhoff, 1987.

[2] B. G. Inman, C. J. Davies, C. R. Torres, and P. J. S. Franks. Deformation of ambient chemical gradients by sinking spheres. *Journal of Fluid Mechanics*, 892:A33, 2020.

[3] Christopher J. Davies and Anne Pommier. Iron snow in the Martian core? *Earth and Planetary Science Letters*, 481:189–200, 2018.